Bacterial Cells Response to Osteogenic Nanopatterns

Dwisetya S Widyaratih (4491408)

TUDelft
Delft University of Technology

Challenge the future

Bacterial Cells Response to Osteogenic Nanopatterns

By

Dwisetya Safirna Widyaratih

in partial fulfilment of the requirements for the degree of

Master of Science
in Biomedical Engineering

at the Delft University of Technology,
to be defended publicly on 27th of September 2017 at 16.00

Supervisor:	Lidy Fratila-Apachitei	TU Delft
	Cornelis W. Hagen	TU Delft
	Peter-Leon Hagedoorn	TU Delft
	Amir A. Zadpoor	TU Delft

Biomaterials and Tissue Biomechanics Section
Biomechanical Engineering Department
Faculty of Mechanical, Maritime, and Materials Engineering
Delft University of Technology

This thesis is confidential and cannot be made public until 27th of September 2022

An electronic version of this thesis is available at http://repository.tudelft.nl/.

TUDelft

Acknowledgements

Abstract

The presence of implants in the body is frequently associated with a high risk of peri-implant infections. The host and the bacterial cells compete to adhere and grow on the implant surface. Therefore, producing an implant that can promote the stem cells function (e.g., osteogenic differentiation) while reducing bacterial colonization is vital. By applying controlled topography on the surface, the behavior of stem cells and bacteria can be influenced. In this study, early interactions between bacteria and osteogenic nanopatterns were investigated. Five different nanopatterns were produced by electron beam induced deposition. The nanopatterns were then incubated with *E. coli K12* strain for 18 hours. Thereafter, the samples were investigated by scanning electron microscope to assess the morphology and the adhesion of bacteria. Based on the experimental results, most of the nanopatterns exhibited a positive effect in reducing bacterial cells adhesion. Moreover, two nanopatterns with heights of 130 nm and 60 nm exhibited bactericidal properties. Possible bactericidal mechanisms have been proposed based on closer examination of the bacteria-nanopattern interface and computational analysis of the interfacial forces. This study investigated the effects of osteogenic nanopatterns on bacterial cells response for the first time. The findings suggested that nanopatterns with both osteogenic and antibacterial properties may be developed for bone implant applications.

Contents

1
Introduction

The presence of implants in the body is frequently associated with a high risk of peri-implant infections, which have disastrous consequences for the patients. The infection is caused by bacteria and can happen during the time of surgery, or anywhere from weeks to years after the surgery [1]. When the implant is first inserted into patient's body, the host and the bacterial cells compete to adhere and grow on the implant surface. If the bacteria first colonize the implant surface, they can develop biofilm, which is resistant to antibiotics and leads to inflammatory host cell responses [2]. In some cases, patients who have a peri-implant infection undergo a revision surgery where the doctor removes some or all parts of the original prosthesis and replace them with new ones. The revision surgery will consume lots of time, effort, and money because it is much more complicated and involves higher risk than the first surgery [3].

Topography or physical patterning of the biomaterial surface has emerged as a promising tool for enhancing the biofunctionality of the implants. Previous studies related to bone implants indicated the potential of controlled nanoscale topography to induce osteogenic differentiation of stem cells [4]. The results showed that the cells on certain patterns had a better adhesion and higher production of mineralized bone matrix than on the planar surface. However, while the patterns were successful at enhancing osseointegration, bacteria interactions with the same surfaces have not been studied. The major challenge is to create nanotopographies that promote different response between host and bacterial cells. Namely, the surface should promote the host cells function while reducing bacterial colonization (Figure 1-1). The current research about cells and bacteria interactions with surfaces is not systematic and not related to each other.
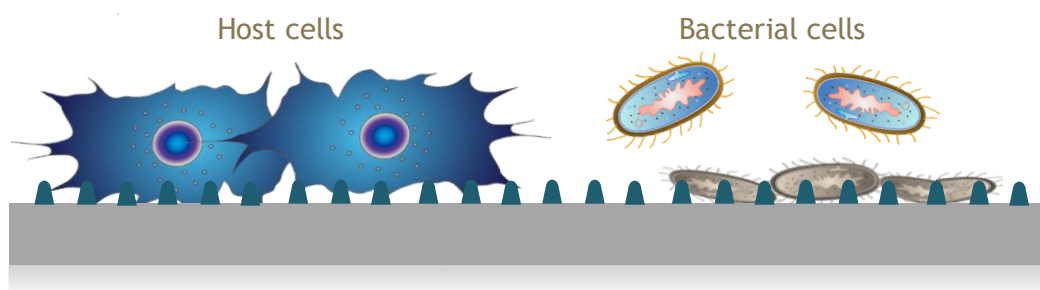

Figure 1-1 The pattern induces a distinct response between host and bacterial cells. The host cells are expected to adhere and differentiate on the pattern while bacterial cells should die or not adhere on the pattern. The images of the cells and bacteria were adapted from Togopic [5]

Therefore, in this thesis, the effects of selected osteogenic nanopatterns were systematically investigated for their effects on bacteria. The scope was limited for bone applications, which involves the adhesion, osteogenic differentiation, matrix formation, and mineralization of mesenchymal stem cells (MSCs) or osteoprogenitor cells (OPGs). The patterns investigated in the study were nanoscale pillars with controlled features dimension and arrangements. From the literature study on MSCs and bacterial cells response to nanotopography, a general trend of the nanopillars in enhancing the stem cell differentiation and reducing bacteria attachment was acquired (Table 1-1).

Table 1-1 The most effective feature size of the pillars in enhancing MSCs osteogenic differentiation and reducing bacteria attachment. The most influencing factors are written in bold.

Cell type	Stem cells	Bacterial cells
Diameter of pillars	~20 - 30 nm	<200 nm induced cell death
Height of pillars	**14 – 33 nm**	~180 nm – 5 µm
Interpillar spacing	~40 nm	**200 – 500 nm**

For the MSCs, adhesion and differentiation are closely linked to pillar height. Several studies showed that stem cells tended to adhere and differentiate on patterns with 14-33 nm height [6-10]. Moreover, it has been known that spatial arrangement significantly affected the behavior of the MSCs. Pits with interspace of 300 nm with ±50 nm displacement has been proven in promoting stem cells osteogenic differentiation [11].

From the bacteria point of view, the most prominent effect is interpillar spacing. An interspace ranging from 200 to 500 nm showed the greatest reduction in bacterial attachment [2,12,13]. The pillar spacing is associated with the bacteria dimensions. The bacteria tend to adhere to pillars with the spacing higher than their size (>500 nm). However, if the pillars spacing is much lower than the size of bacteria, the surface area and the adhesion site for the bacteria are increased and consequently bacterial adhesion is promoted. Another parameter that influences bacteria adhesion is the aspect ratio of the pillars. Patterns with aspect ratios greater than 1 can result in cell death [14-16]. Moreover, by using sharp pillars, the bactericidal activity can be enhanced. When adhering on the pattern, the bacteria have to stretch. However, the cell walls of the bacteria are not elastic enough to follow the topography and lead to membrane rupture [17,18]. One example is represented by the wings of the Clanger cicada (*P. claripennis*), which are naturally occurring bactericidal surfaces. The wing surfaces are covered by an array of nanopillars with interspace of 170 nm, height of 210 nm, base diameter of 100 nm, and a spherical cap of 60 nm in diameter. The surface was lethal to *P. aeruginosa, B. subtilis, P. maritimus*, and *S. aureus* [18,19].

According to these findings, two osteogenic nanopatterns were first considered for investigation. The first pattern (OST1) was reproduced from the study conducted by Sjostrom *et al.* [6], which had 28.1 ± 3.48 nm diameter, 15.4 ± 4.19 nm high, and 40.1 ± 3.87 nm center-center distance. The second pattern (OST2) involved controlled disordered nanostructures with interspace of 300 nm. Furthermore, three different variations of the OST2 nanopattern were included to evaluate the effect of pillars arrangement, height, and diameter.

The nanopatterns generated in this thesis were fabricated using electron beam induced deposition (EBID). This technique is an excellent candidate for exploring a new range of geometries and sizes for preliminary cell studies [20]. EBID is very flexible because it can directly deposit the material without additional processing, and image the result *in-situ*. Moreover, the process is maskless and does not rely on the use of resist. It has a magnificent performance in producing complex patterns, shapes, and arrangements in the nanoscale and has been successful in making high-resolution nanopatterns. Afterwards, the nanopatterns were cultured with *E. coli* for 18 hours in Lysogeny-broth (LB) medium. The samples were then examined by scanning electron microscope (SEM) to assess bacterial cells adhesion and morphology. In addition, computational modelling of the pillars was performed to estimate forces and pillars deflection exerted by the bacteria. By analyzing all of the results, the possible mechanisms of bacterial cells attachment and death will be discussed in this report.

2

Materials and Methods

2.1 Nanopatterns Generation by EBID

2.1.1 Substrate Preparation

The substrate used for the experiment was single side polished silicon wafer (4 inches, thickness 525 ± 25 μm, (100), 1-side polished, p-type, 0-100 Ohm cm). The silicon wafer is commercially available, easy to handle, and has sufficient electrical conductivity for SEM and EBID process. It has been used in cells studies and proven to be sufficient for *in vitro* testing [21]. The silicon wafer was diced into 1x1 cm^2 to fit inside a 24-well plate. In order to minimize the dirt and contaminants on the surface, the wafers were soaked in nitric acid for 15 minutes and rinsed with deionized water. The samples were dried with compressed nitrogen gas and put into the oven with the temperature of 90°C to make sure the samples were perfectly dry.

2.1.2 Nanopatterns Definition

There were in total seven surfaces, including two control surfaces and five patterned surfaces (Figure 2-1). Silicon wafer (CTR1) and thin layer of EBID deposits (CTR2) were investigated to assess the effect of surface chemistry on the bacteria. There were two main patterns designed in this thesis. The first pattern, OST1, had sizes of 28 nm diameter, 15 nm high, and 40 nm interpillar spacing. The second pattern, OST2, had 300 nm center-center distance with ±50 nm controlled disordered (Figure 2-2b). The diameter and height of the pillars were 120 nm and 130 nm, respectively. In order to evaluate the effect of pillars arrangement, height, and diameter, three different variations of the OST2 pattern were included. In the first variation, disordered (OST2) and square arrangement (OST2-SQ) was compared (Figure 2-2). In the second and third variation, the height and diameter of the pillar were changed to 60 nm (OST2-H60) and 50 nm (OST2-D50), while the other features were kept constant. The schematic representation of the nanopatterns is depicted in Table 2-1.
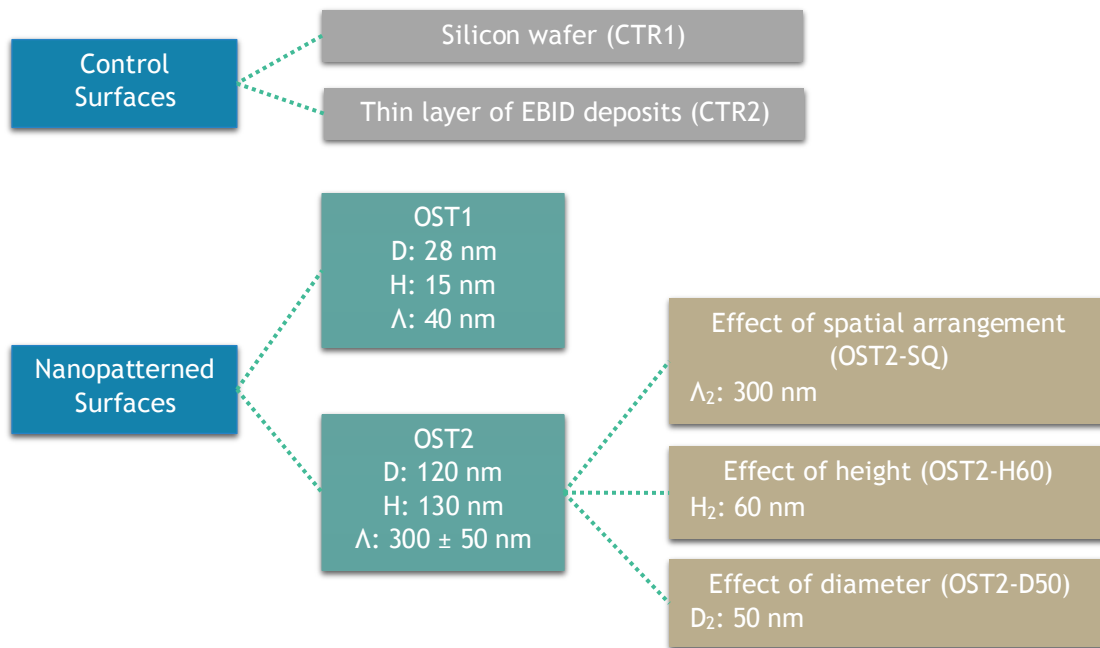
Figure 2-1 An overview of the surfaces produced for bacterial testing. D represents diameter, H represents height, and λ represents the interspace of the pillars.
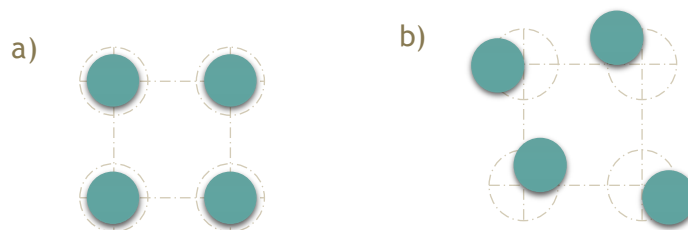
Figure 2-2 Difference between square arrangement (a) and controlled disordered arrangement (b). In the disordered arrangement, the pillars were ±50 nm away from the true center

Table 2-1 Schematic representation of the nanopatterns (cross-sectional and top view)

2.1.3 EBID Conditions

All experiments were performed using the Nova NanoLab 650 Dual Beam system (FEI, Oregon) (Figure 2-3 a). EBID was performed in ultrahigh resolution (immersion mode) with a 20 kV electron beam. The background vacuum of the system was 1-3 x 10^{-6} mbar, and the EBID process started at 4-6 x 10^{-6} mbar. The working distance was

approximately 5 nm. Trimethyl(methylcyclopentadienyl)-platinum(IV) $(((CH_3C_5H_4)Pt(CH_3)_3$, $MeCpPt^{IV}Me_3$ or $C_9H_{16}Pt)$ gas precursor (Figure 2-3 b) was used for the experiment because it is stable and widely used [22]. The deposits typically consist of carbon (90%) and Pt (10%) [23]. The gas nozzle was inserted in every experiment and located 140 µm above the irradiated area. More details about the method are included in Appendix A.
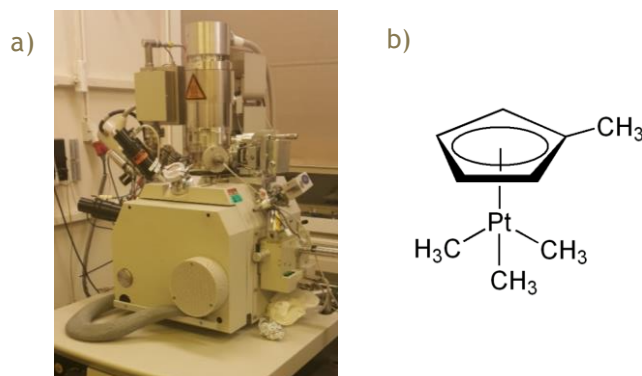
Figure 2-3 (a) Nova Nano Lab 650 Dual Beam system and (b) $C_9H_{16}Pt$ precursor

The patterning was done in single dot exposure and electron-limited regime. Table 2-2 shows the patterning parameters for each array of pillars. For the OST2-D50 nanopattern, a lower value of beam current was used to reduce the beam diameter. For OST2-H60 nanopattern the beam was defocused for 5 µm in the writing process. Defocus causes a wider beam, and however, it causes a lower vertical growth [24].

Table 2-2 Final EBID settings that were used for the patterns. Where the I_{beam} represents the beam current, t_{dwell} represents the dwelling time, $t_{refresh}$ represents the refresh time.

Type	I_{beam}	Array	t_{dwell}	$t_{refresh}$	Repeats	Passes	Exposure time / pillar	Total duration
OST1	2.4 nA	160x160	0.1 ms	3 µs	100	1	10 ms	4:24 min
OST2	2.4 nA	23x23	3 ms	3 µs	50	3	450 ms	3:58 min
OST2-SQ	2.4 nA	23x23	3 ms	3 µs	50	3	450 ms	3:58 min
OST2-H60	2.4 nA	23x23	8 ms	3 µs	50	1	400 ms	3:32 min
OST2-D50	39 pA	23x23	25 µs	3 µs	500	100	1,250 ms	12:21 min

The focused electron beam was controlled by using a stream file. The stream file was generated by Matlab where the coordinates of all pixels were acquired and generated. The stream file only wrote in a given area ranging from 0 to 4095 pixels for X coordinate, and 280 to 3816 pixels on the Y coordinates. Magnification of 15,625x was used for patterning (1 pixel equals to 2 nm), resulting in a maximum total area of approximately 8.1 µm x 7 µm. In order to pattern a larger area, the stage had to be moved and the stream file was written in a serpentine writing strategy (Figure 2-4).

Stream file

Figure 2-4 Step and repeat process for increasing the total area of patterning.

In order to evaluate the effect of surface chemistry of the pattern on bacteria, a thin layer of platinum-carbon was deposited on top of the silicon substrate. $C_9H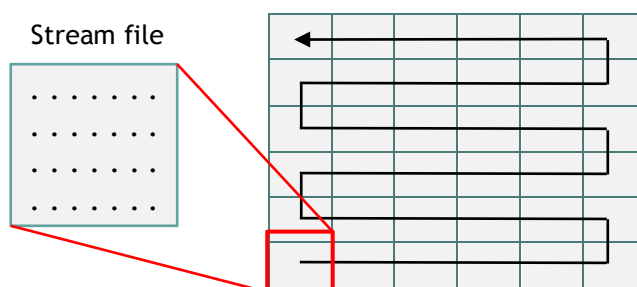_{16}Pt$ gas precursor was pumped into the chamber while performed imaging by SEM. In this manner, the collision between the electron and the gas resulted in a thin homogeneous layer of platinum-carbon (Pt-C). The scanning was performed in a raster direction with a dwell time of 1 ms (Figure 2-5). The magnification was set to 2,000x and covered 60 x 60 μm^2 area (Table 2-3).

Table 2-3 EBID parameters used for deposition

Area	3,600 μm^2
Magnification	2,000 x
Scanning dwell time	1 ms
Duration	16 minutes
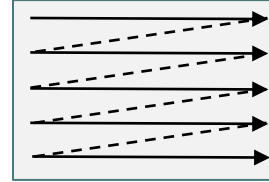
Figure 2-5 Raster scan

2.1.4 Nanopatterns Characterization

After writing, the precursor gas was pumped out of the chamber. The nanopatterns were imaged after leaving overnight in the chamber to minimize the contamination. The diameter and height of the structures were obtained from the SEM measurement using 35° tilting (Figure 2-6).
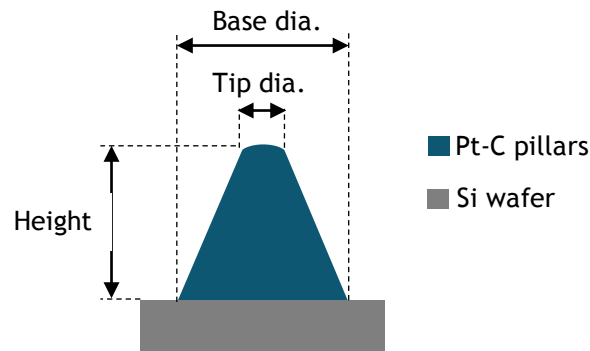
Figure 2-6 Pillars characteristics were estimated from SEM images. The diameter was measured at the base and the top of the pillar. The height was measured as a tangent line from the base to the tip.

In order to measure the contact angle of CTR1 and CTR2 surface, Drop Shape Analyzer DSA 100 (Kruss, Hamburg) was utilized. The fluid used in the experiment was distilled water. Static testing was performed with 100 µl/min rate and volume of 4 µl. Afterwards, the contact angle of the nanopatterns was approximated using Carrie-Baxter model [25]. It was assumed that air was trapped between the pillars and the hydrophobicity of the patterns would increase (Figure 2-7). The Cassie-Baxter contact angle (θ_c) is given by

$$cos\theta_c = \varphi \ (cos\theta_o + 1) - 1 \qquad \text{(Eq. 1)}$$

Where φ and (θ_o) are solid fraction and contact angle on smooth surface. The solid fraction was defined by the ratio between tip area of the pillar and the projected surface area. The tip was assumed to be flat and in contact with the liquid [26].

$$\varphi = \frac{A_{tip}}{A_{projected}} = \frac{\pi \, d^2}{4 \, i^2} \qquad \text{(Eq. 2)}$$

Where d is the tip diameter of the pillars and i represents the interspace.
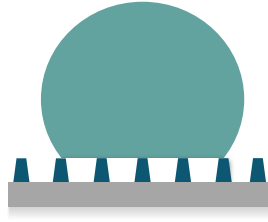
Figure 2-7 Schematic representation of behavior of the drop on nanopatterned surface according to Cassie-Baxter model

2.2 Bacterial Cultures

2.2.1 Bacterial Strain and Growth Conditions

Escherichia coli (K-12 strain), a rod-like Gram-negative bacterium, was used in this experiment. *E. coli* is one of the pathogens in orthopedic implant infection [1]. It also has been extensively studied and used as a model organism. It is able to proliferate rapidly and survive in variable growth condition. Lysogeny-broth (LB) was used to cultivate *E. coli*. LB is a nutritionally rich medium and commonly used for cultivation of *E. coli*. LB was produced from 1% bacto-tryptone, 0.5% bacto-yeast extract and 1% NaCl in demineralized water. To solidify the liquid medium, 15 gram/liter of bacto agar was added and autoclaved at 121°C.

A loop of bacteria stock was streaked onto Lysogeny-broth (LB) agar plate and incubated overnight at 37°C. A single homogeneous colony was picked and then grown overnight in liquid LB medium at 180 RPM and 37°C. Before starting the experiment, the silicon wafer samples were soaked with ethanol and sterilized under UV light for 20 min. The sterilized samples were then placed in 24-well cell culture plates. Then, 0.5 mL of LB medium was added to the well to enhance the wetting. The optical density of the overnight culture was measured by using absorption spectroscopy at a wavelength of 600 nm (OD_{600}). The culture was then diluted in LB medium to OD_{600} = 0.1 and transferred to the 24-well plates (0.5 mL for each well), resulting in a final mixture of OD_{600} = 0.05. The bacterial cell suspension was mixed at 100 rpm for 5 min and then incubated at 37°C for 18 hours. After incubation, the samples were rinsed one time and shaken at 50 rpm for 5 min with 0.01 M phosphate-buffered saline (PBS), pH 7.4. PBS is a common buffer used for dilution of culture media and cleaning of cell cultures because it is isotonic and non-toxic for cells. The process sequence of the experiment is illustrated in Figure 2-8. Preliminary experiments for developing the culturing protocols are included in Appendix B.
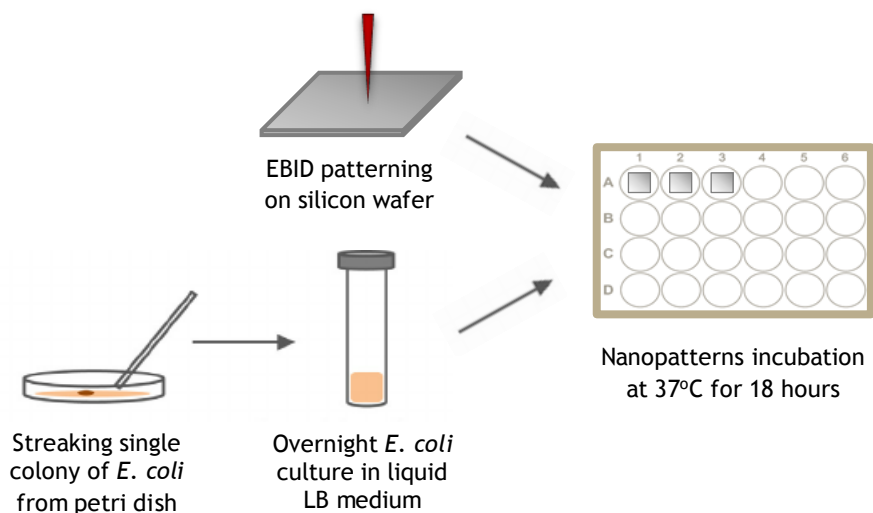
Figure 2-8 Process sequence of the experiments. The nanopatterns were produced by EBID, while bacterial pre-culture took place by using agar and liquid medium. The nanopatterns were then incubated with the *E. coli* suspension.

2.2.2 Samples Preparation for SEM Analyzes

Before performing SEM investigation, the samples were fixed and dried. The samples with adherent bacteria were first preserved in a fixation solution containing 4% formaldehyde and 1% glutaraldehyde in 10 mM phosphate buffer, pH 7.4 for 2 hours at 4°C. After that, the samples were washed in MiliQ water for 10 minutes and dehydrated using a series of ethanol washings: (1) 50% ethanol for 15 minutes, (2) 70% ethanol for 20 minutes, and (3) 96% ethanol for 20 minutes. Finally, the samples were soaked in chemical drying agent, hexamethyldisilazane (Sigma-Aldrich, Missouri), for 30 minutes. Lastly, the samples were dried in air and sputter coated with gold to enhance conductivity.

2.2.3 Scanning Electron Microscopy of the Cultures

The bacteria grown on the samples were characterized by SEM. All the images were acquired by Nova Nano Lab 650 Dual Beam system (FEI, Oregon). Samples were positioned at a working distance of approximately 5 mm. The acceleration voltage and beam current were 5 kV and 0.4 nA.

From the SEM images, morphology and density of bacteria were acquired. The morphology included cell length, cell width, and projected extracellular polymeric substance (EPS) area (Figure 2-9a). By using Gwyddion 2.47 image analysis software, the projected area of bacteria and secreted EPS can be computed. The EPS area was expressed as the percentage increase relative to projected area of the bacteria. The density was determined based on the cell counting on the surrounding control area (silicon wafer) and patterned area (Figure 2-9b).
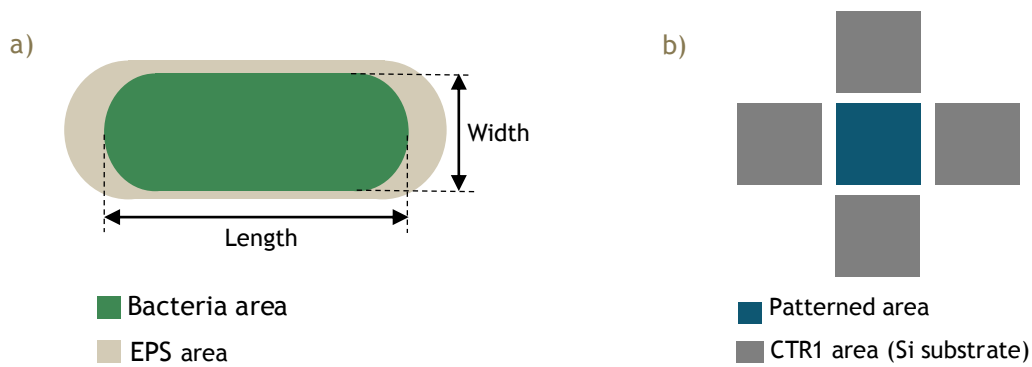
Figure 2-9 (a) Measuring the cell length, cell width, and projected area of bacteria and EPS, and (b) Comparing cell density on the patterned area and the surrounding control area.

Additionally, the damaged and dead cells were also counted to estimate the bactericidal efficiency of the patterns. It was expressed as the ratio between the damaged cells and the total number of cells on the pattern. The bacteria was considered as damaged if the wrinkling and deformation occurred on the cell surface (Figure 2-10).
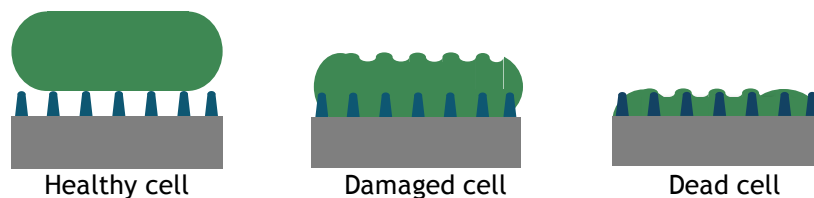
Figure 2-10 Schematic representation of healthy, damaged, and dead bacterium. Healthy cell can maintain its rod-like shape. Wrinking and deformation occur on damaged cell. Dead bacterium shrunk and flatten.

Finally, the obtained data were analyzed using one-way ANOVA and one-way MANOVA using SPSS statistical analysis software to determine whether there were any statistically significant differences between the nanopatterns.

2.3 Computational Modelling

Computational modeling by ABAQUS 6.14-5 was performed to understand the interfacial forces and pillars deflection. In the model, the 3D deformable geometry was defined based on the measurement of the pillars feature. The Young's modulus of the material was assumed to be 25 GPa [27], with Poisson's ratio of 0.25 [28]. The properties of $C_9H_{16}Pt$ deposits were not found in the literature. However, these assumptions were made based on the hydrogenated amorphous carbon deposits. Quadratic tetrahedral C3D10 element was chosen because it had more flexibility for meshing the curvature of the structure. Boundary condition was applied on the bottom of the pillars in all directions and rotations. On top of the pillar, forces in X-direction was applied (Table 2-4). It was assumed that the forces were shear forces and constant for all nanopatterns.

Table 2-4 Load applied in the model is represented by the red arrow

OST1	OST2	OST2-SQ	OST2-H60	OST2-D50
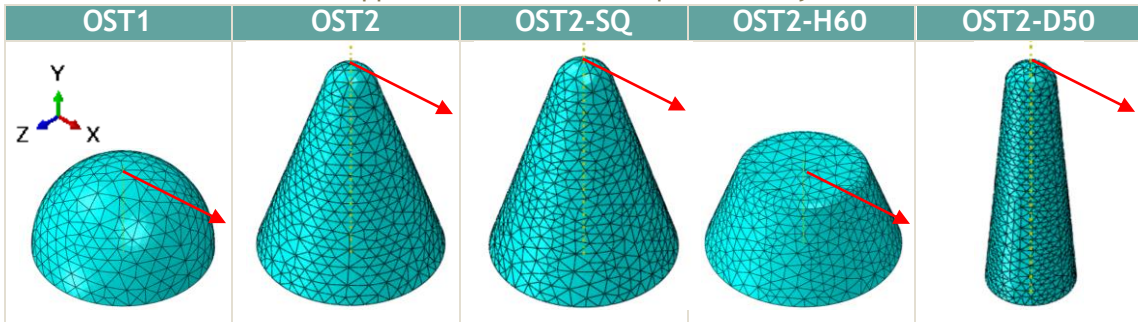
The value of forces exerted by the bacteria was acquired from the modeling of OST2 nanopattern. Firstly, the maximum deflection of OST2 pillars was determined from SEM images. Then, the forces were acquired by applying the deflection to the OST2 model. Finally, the forces obtained were implemented for all other nanopatterns types. The result obtained from the modeling was the deflection of the nanopillars. The process of the modelling is illustrated in Figure 2-11.
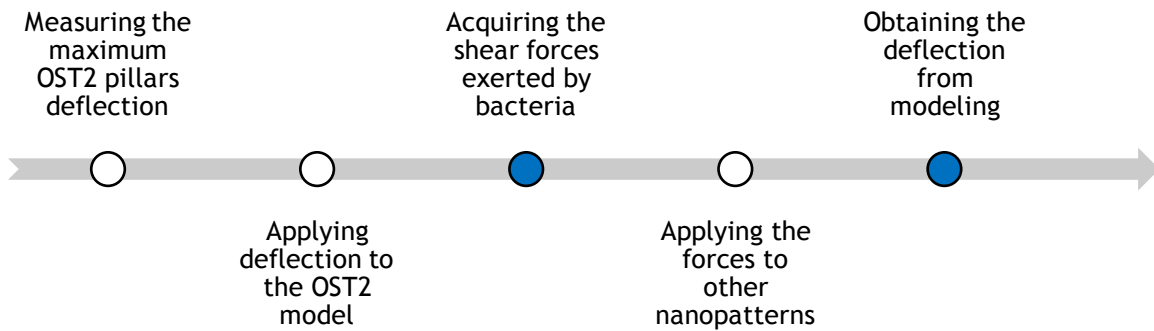
Figure 2-11 Computational modeling process. The data obtained from the modeling are represented in blue dots.

12

3
Results

3.1 Fabrication and Characterization of Nanopatterns

3.1.1 OST1 Nanopattern

The OST1 nanopattern was successfully reproduced by EBID. (Figure 3-1a). The measured dimensions of these patterns are provided in the Table 3-1. In the study by Sjostrom *et al*. [6], their patterns were fabricated by using through mask anodization (Figure 3-1b). The process produced a larger deviation regarding the sizes and interpillar spacing than the nanopattern made by EBID. On the other hand, EBID has more control over shape, feature size, and interspace.
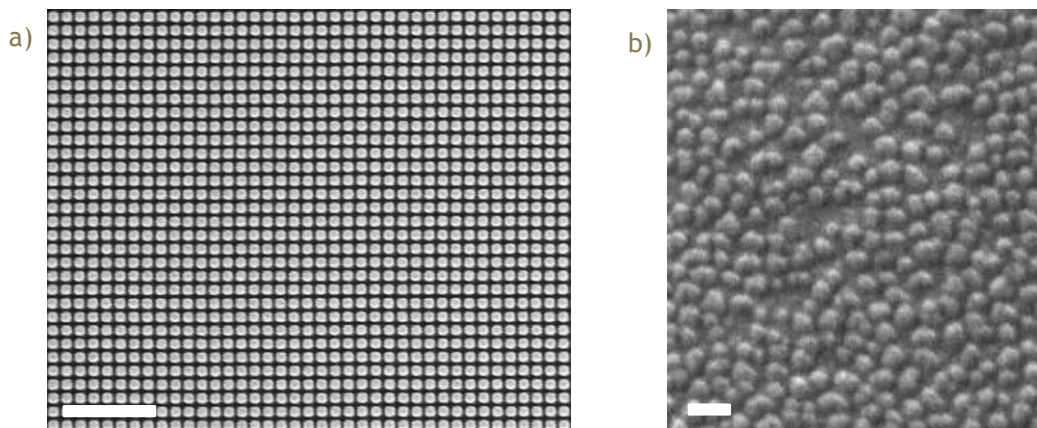
Figure 3-1 (a) SEM image of OST1 pattern (scale bar 250 nm). (b) SEM image of titanium oxide nanopillars produced by Sjostrom *et al*. [6]

Table 3-1 Diameter, height, and interspace of nanopattern made by EBID (OST1) and by Sjostrom *et al*. [6]

	Diameter (nm)	Height (nm)	Interspace (nm)
OST1	27.95 ± 1.17 nm	14.63 ± 1.16 nm	40.44 ± 1.96 nm
Sjostrom [6]	28.1 ± 3.48	15.4 ± 4.19 nm	40.1 ± 3.87 nm

3.1.2 OST2 Nanopatterns

The OST2 nanopatterns had controlled disordered and larger features size relative to OST1. The SEM results were represented in Figure 3-2. Variations were produced from the basic pattern, which includes: 1) Ordered pattern (OST2-SQ); 2) Disordered pattern with pillar height of 60 nm (OST2-H60); and 3) Disordered pattern with diameter of 50 nm (OST2-D50) (Figure 3-2). The measured dimensions of these nanopatterns are provided in the Table 3-2.

OST2

SQ
Effect of arrangement

H60
Effect of height

D50
Effect of diameter
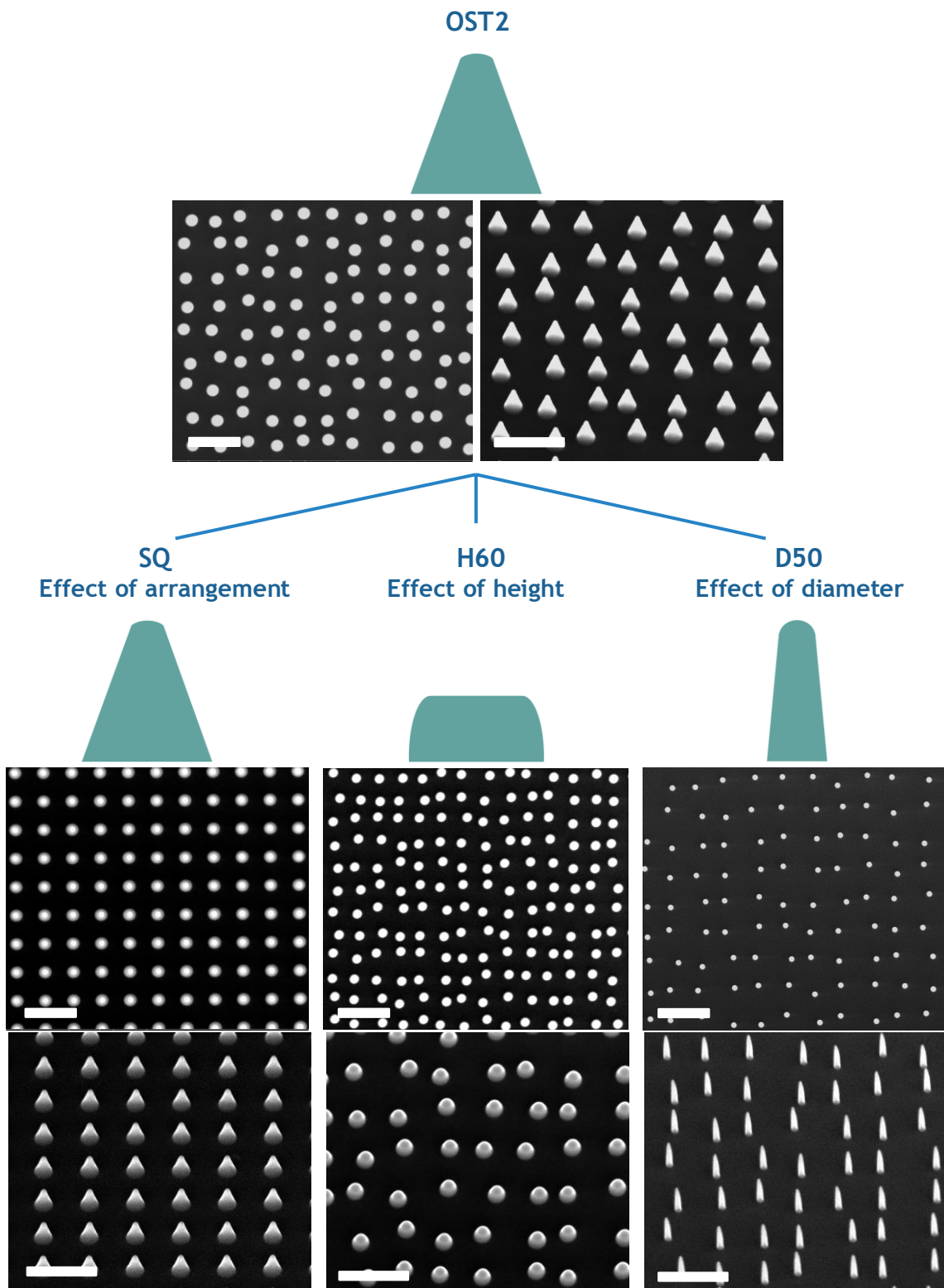
Figure 3-2 Schematic representation of the OST2 patterns profile, followed by top and 35°
tilted SEM images of OST2 nanopatterns (scale bar 500 nm). The OST2 nanopattern has three
variations, which are ordered arrangement (SQ), 60-nm high pillar (H60), and 50-nm diameter
(D50)

14

Table 3-2 Diameter, height, interspace, and aspect ratio of the OST2 pattern and its derivatives (SQ, H60, and D50)

	Diameter (nm)	Height (nm)	Interspace (nm)	Aspect ratio
OST2	122.34 ± 22.39 (base) 31.80 ± 3.28 (tip)	128.02 ± 5.39	300 ± 50	1.05
OST2-SQ	123.79 ± 5.87 (base) 35.09 ± 2.31 (tip)	131.91 ± 6.16	298.62 ± 4.09	1.07
OST2-H60	126.13 ± 8.18 (base) 77.12 ± 6.45 (tip)	57.20 ± 5.22	300 ± 50	0.45
OST2-D50	49.05 ± 3.79 (base)	129.66 ± 9.54	300 ± 50	2.64

Despite OST2 and OST2-SQ nanopatterns were produced by the same patterning conditions, the OST2 has a greater variation in the base diameter. Due to the ± 50 nm displacement, the distance between pillars is not identical. The pillars that have a smaller gap could experience a greater proximity effect, resulting in tremendous growth of the adjacent pillars. A different cross-section profile was acquired from H60 nanopattern. The deposits had a flat top. Defocused was applied for the beam, resulting in lower vertical growth and broader diameter of the deposits.

3.1.3 Surface Contact Angle

The two control surfaces were firstly characterized by drop shape analysis. The silicon wafer had a contact angle of 23.80 ± 2.97^{o} and the Pt-C surface was 43.32 ± 3.00^{o}. Thereafter, using Cassie-Baxter model [25], the changes in surface contact angle due to the pattern were estimated. The value of solid fraction was calculated by assuming that the nanopillars have a flat top (Table 3-3). The presence of nanopatterns led to hydrophobic properties on the surfaces for both chemistries.

Table 3-3 Contact angle of the silicon and Pt-C nanopatterns based on Cassie-Baxter model.

Type	Solid fraction	Contact angle (silicon)	Contact angle (Pt-C)
OST1	0.3835	105.41°	109.73°
OST2	0.0088	169.45°	169.98°
OST2-SQ	0.0107	168.36°	168.94°
OST2-H60	0.0519	154.24°	155.55°
OST2-D50	0.0209	163.70°	164.52°

3.2 Bacterial Adhesion and Morphology on Nanopatterned Surfaces

Nanotopographical effect on bacteria was evaluated after 18 hours of incubation. The optical density of the bacteria suspension was measured in every experiment, and it consistently reached OD600 = ~1.4.

3.2.1 OST1 Nanopattern

In the OST1 nanopattern, the dimensions of the pillars were much smaller than the bacteria size, and the nanopillars were densely arranged. Cell morphology and density data are shown in Table 3-4. Representative optical microscope and SEM images are included in Figure 3-3, which suggested that there is no sign of a disturbed

or damaged bacteria on the nanopatterned and control areas. However, the cell density is reduced by up to 35% on the nanopatterned area (Figure 3-3a). Closer examination at the interface between non-patterned and patterned area indicates that the bacteria secrete more EPS on the OST1 area than the surrounding control surface (Figure 3-3b). The EPS surrounds the bacteria and increases attachment area of ~40% (Figure 3-3c).

Table 3-4 Cell length, cell width, percent increase of EPS area, density, and damaged cell of the OST1 nanopattern

Substrate	Cell length (µm)	Cell width (nm)	EPS area (%)	Density	Damaged cell
OST1	2.06 ± 0.61	620.05 ± 67.72	39.35 ± 16.14	62.84%	-
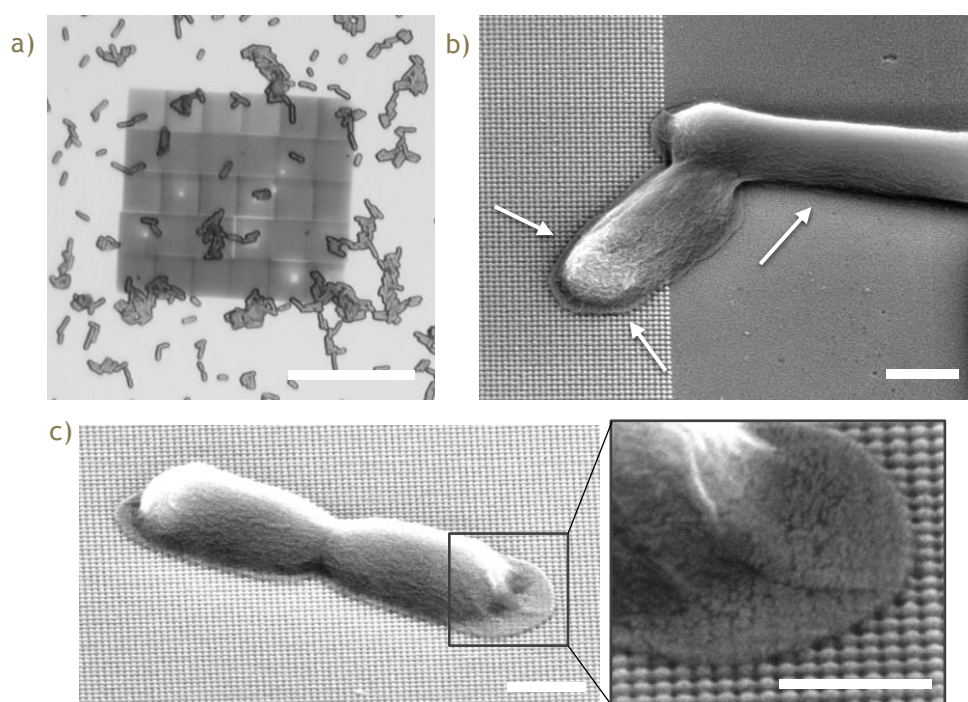
Figure 3-3 (a) Optical microscope image of OST1 nanopattern (scale bar 2 µm). (b) 50º tilted SEM images of *E. coli* on OST1 nanopattern (scale bar 500 nm). The arrows indicate the different EPS spreading between the bacteria on the pattern and CTR1 surface. (c) Attachment of EPS layer on OST1 nanopattern (scale bar of the inset is 300 nm).

3.2.2 OST2 Nanopattern

On the OST2 nanopattern, the height and the interspace of the pillars were much larger than the on OST1 pattern. Cell morphology and density data are shown in Table 3-5. The optical microscope and SEM images are represented in Figure 3-4. It is clearly seen that the OST2 nanopattern significantly reduced the number of bacteria adherent (Figure 3-4a). By the help of EPS, the bacteria "anchor" on the pillars (Figure 3-4b). Some bacteria are not able to divide and just grow very long (Figure 3-4c). Almost ~25% of bacteria on the OST2 nanopillars are damaged. The bacteria are first deformed (Figure 3-4d), then, the bacteria sink onto the pillars and leave behind the cell membrane (Figure 3-4e).

Table 3-5 Cell length, cell width, percent increase of EPS area, density, and damaged cell of the OST2 nanopattern

| Substrate	Cell length (µm)	Cell width (nm)	EPS area (%)	Density	Damaged cell
OST2	1.99 ± 1.22	544.07 ± 96.87	16.52 ± 6.45	22.87%	23.56%
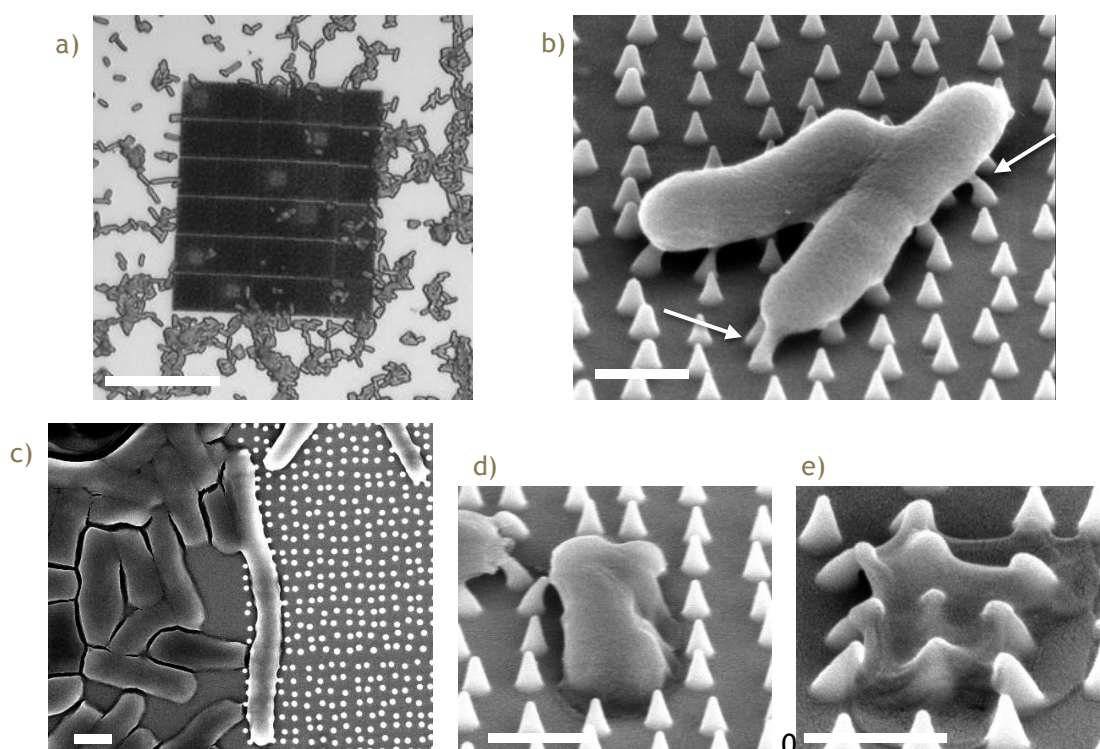
Figure 3-4 (a) Optical microscope image of OST2 nanopattern (scale bar 2 µm). (b) 50° tilted SEM images of *E. coli* on OST2 nanopattern (scale bar 500 nm). The arrows indicate the attachment point of EPS on the pillars. (c) Some bacteria grow very long due to stress. The damage starts when the bacteria deform (d) and sink (e) into the pillars. Then the cytoplasm leaks, leaving only their membrane.

3.2.3 OST2-SQ Nanopattern

The results are represented in Figure 3-5 and Table 3-6. Bacterial density on OST2-SQ pattern is approximately 50% less than the CTR1 area (Figure 3-5a). The bacteria exhibit a similar EPS attachment as the bacteria on the disordered arrangement (Figure 3-5b). There is also some evidence of cell death (Figure 3-5c). Almost 13% of the bacteria adhered on the nanopattern were damaged. Like the OST2 pattern, some bacteria also cannot divide and grow very long (Figure 3-5d).

Table 3-6 Cell length, cell width, percent increase of EPS area, density, and damaged cell of the OST2-SQ nanopattern

| Substrate	Cell length (µm)	Cell width (nm)	EPS area	Density	Damaged cell
OST2-SQ	2.56 ± 1.67	573.66 ± 105.38	14.95 ± 6.66%	58.73%	12.93%
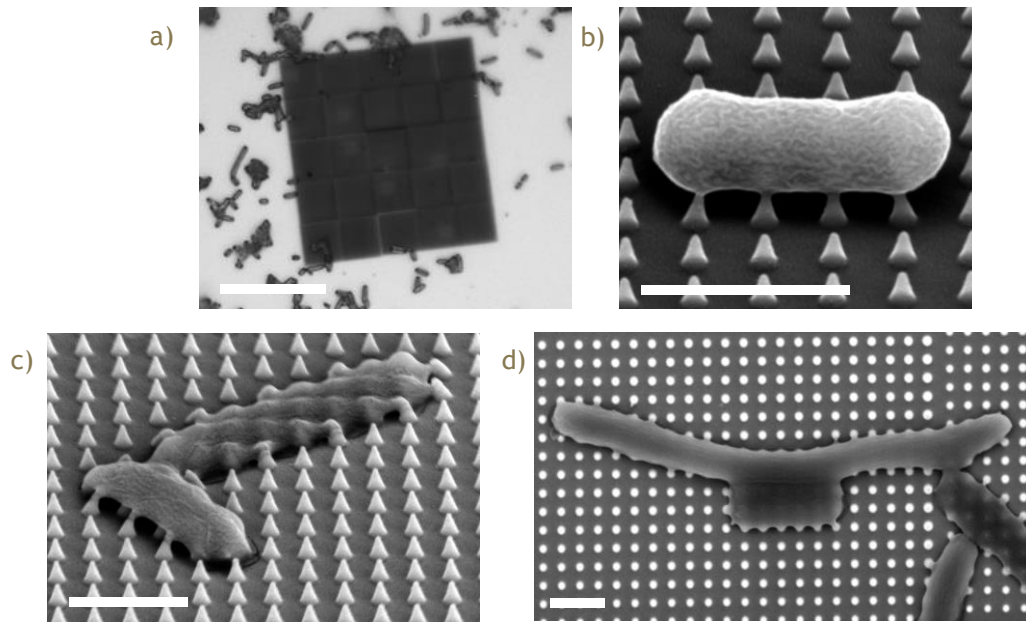
Figure 3-5 (a) Optical microscope image of OST2-SQ nanopattern (scale bar 2 μm). (b) 50° tilted SEM images of *E. coli* on OST2-SQ nanopattern (scale bar 1 μm). Bacteria is anchoring on the pillars. There is some evidence of cell death (c), and some bacteria grow very long (d).

3.2.4 OST2-H60 Nanopattern

On OST2-H60 nanopattern, the pillars had a lower height and different profile relative to the OST2 nanopattern. Figure 3-6 represent optical microscope and SEM images and Table 3-7 summarizes the quantification result of the SEM images. The results show that the cell density only reduced by ~13% (Figure 3-6a). Unlike the other OST2 nanopatterns, the EPS on the OST2-H60 nanopattern is spread around the cell without having any disturbance (Figure 3-6b). Remarkably, this surface has a similar efficiency as OST2 nanopattern in killing bacteria, which is 22%. Many bacteria have a wrinkling shape (Figure 3-6c), and even a flatten membranes (Figure 3-6d).

Table 3-7 Cell length, cell width, percent increase of EPS area, density, and damaged cell of the OST2-H60 nanopattern

| Substrate	Cell length (μm)	Cell width (nm)	EPS area	Density	Damaged cell
OST2-H60	2.24 ± 0.71	709.98 ± 68.57	26.84 ± 8.03%	87.35%	22.64%
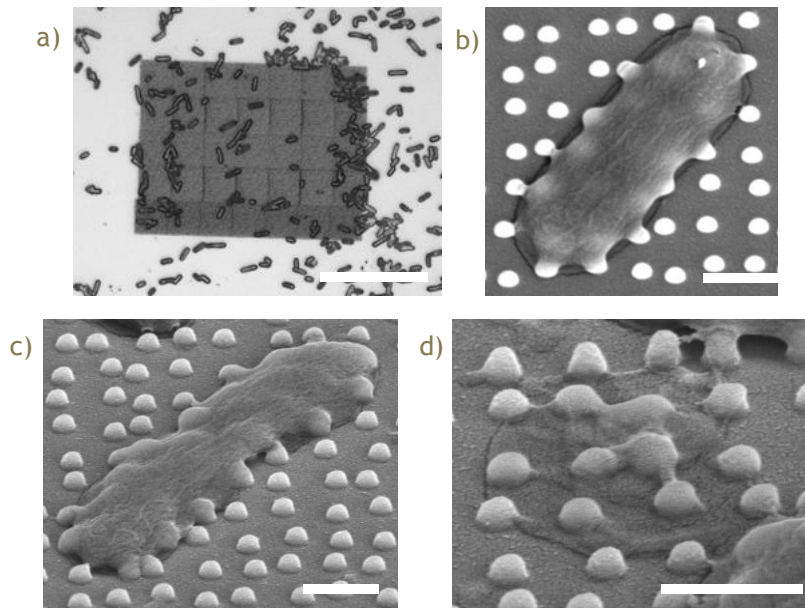
Figure 3-6 (a) Optical microscope image of OST2-H60 nanopattern (scale bar 2 μm). (b) 50°
tilted SEM images of *E. coli* on OST2-H60 nanopattern (scale bar 500 nm). The EPS can spread
around the bacteria. A deformed (c) and dead (d) bacteria point out that the surface has
bactericidal properties.

3.2.5 OST2-D50 Nanopattern

Figure 3-7 and Table 3-8 represent the results of bacterial cells incubation on
OST2-H60 nanopattern. There is a noticeable reduction in bacterial adhesion on OST2-
D50 nanopattern (Figure 3-7a). The bacterial density on the pattern is less than 30% of
the CTR1 surface. Unfortunately, the effect of diameter on bactericidal effect could
not be fully assessed due to bending of the pillars (Figure 3-7b) and failure (Figure
3-7c). The SEM image suggests that the attachment and movement of bacteria caused
the pillars bending (Figure 3-7d).

Table 3-8 Cell length, cell width, percent increase of EPS area, density, and damaged cell of
the OST2-D50 nanopattern

Substrate	Cell length (μm)	Cell width (nm)	EPS area	Density	Damaged cell
OST2-D50	2.31 ± 0.94	533.41 ± 71.74	22.72 ± 20.54%	28.14%	-
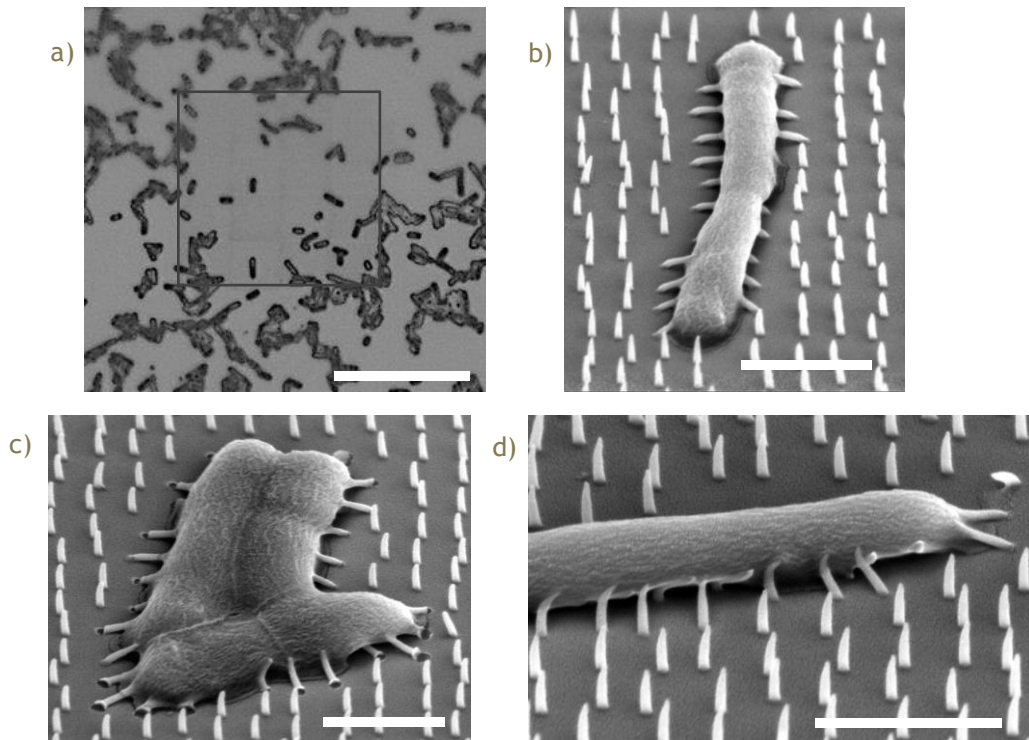
Figure 3-7 (a) Optical microscope image of OST2-D50 nanopattern (scale bar 2 μm). The square indicates the area of the nanopattern (b) 50° tilted SEM images of *E. coli* on OST2-D50 nanopattern (scale bar 1 μm). The pillars are displaced due to bacterial adhesion. (c) The pillars were collapsed and detached from silicon wafer substrate. (d) The movement of bacteria caused the pillars under the bacteria bend.

The quantified results from the SEM images are included in Figure 3-8. By looking at the density of the cells, all of the nanopatterns, except OST2-H60, showed a significant effect in reducing bacterial adhesion. Amongst all the patterns, the OST2 is very efficient in reducing bacterial adhesion. The bactericidal properties were occurred on the OST2, OST2-SQ, and OST2-H60 nanopatterns. The most deadly surface is OST2, followed by OST2-H60. The morphology of the bacteria on the nanopatterns is diverse for each nanopattern. However, the graph implies a wider variety of cell length on OST2, OST2-SQ, and OST2-D50 patterns. It is suggested that higher pillar will generate stress for the *E. coli* and disturb the cells division. Besides, it is clear that the area of EPS on the OST1 is broader than the OST2.

Figure 3-8 Graphs illustrate ratio of damage cells, ratio of cell density, cell length, cell width, and percent increase of EPS area between controlled and patterned surfaces. The symbols represent the different p value (* = p<0.05, ** = p<0.01, *** = p<0.001).

3.3 Computational Modelling of the Nanopillars Deflection

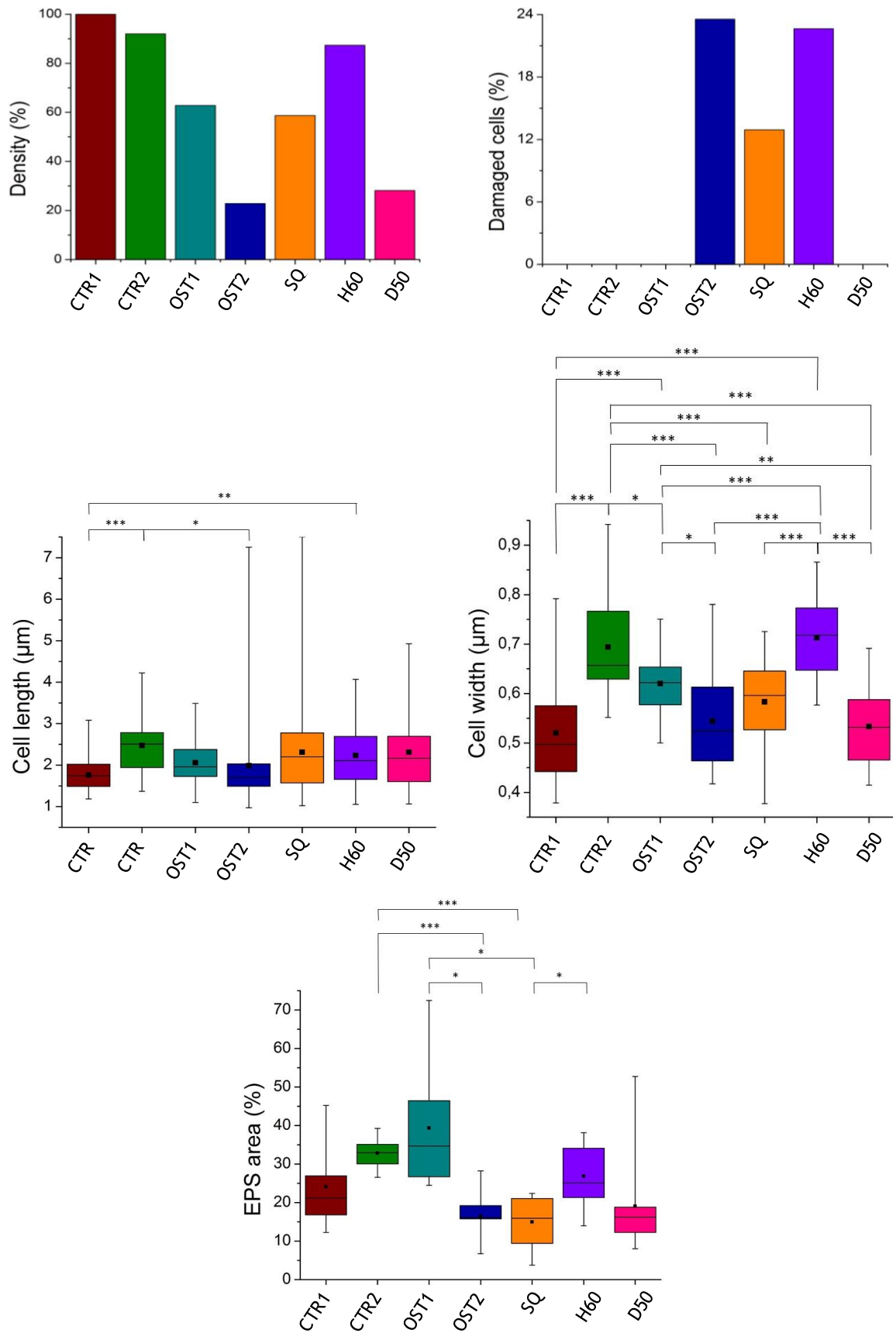Based on the computational modeling, the forces experienced by the nanopillars were 3.198 µN. It was assumed that all the pillar types experience the same amount of forces. Table 3-9 and Figure 3-9 represent the computational result for the OST2 pattern and its derivatives. It must be noted that these modelings are simplification of the mechanism of *E. coli* and EPS attachment on the nanopillars. The value was roughly calculated and still needs further investigation.

Figure 3-9 Comparison between OST2, OST2-SQ, and OST2-H60 nanopillar deflections in the simulation and SEM images (50° tilted view with scale bar of 250 nm)

Table 3-9 Forces and deflections of OST2 nanopattern and its derivatives acquired from the simulation

Pillar type	OST2	OST2-SQ	OST2-H60	OST2-D50
Maximum forces	3.198 µN	3.198 µN	3.198 µN	3.198 µN
Maximum deflection	116.20 nm	103.20 nm	4.08 nm	856.70 µm

In the simulation of OST2-D50 pillar, a tremendous deflection appeared. The results suggest that the sizes and the properties of the pillar cannot withstand the forces. The frustum-like shape is the sturdiest structure because the forces can be distributed over the flat area. The OST2-H60 pillar is able to maintain its shape and only experiences insignificant bending. The bending is highly influenced by the feature size of the pillars. Larger deflection will occur on smaller diameter and/or higher pillar.

By observing the SEM images of OST2-D50 pillars, fracture of the pillar does not appear. Instead, the failure was developed on the adhesion site between EBID deposits and silicon wafer (Figure 3-10a). The pillars, which receive a higher forces from the EPS, are detached from the silicon surface. The reaction forces on the bottom of the pillars may explain why the pillars were detached from the silicon substrate. The reaction force of OST2-D50 (Figure 3-10b) is enormous and nearly 10-fold greater than OST2 (Figure 3-10c). This results suggest that the adhesion between platinum-carbon and silicon wafer is not strong enough. An alternative way to tackle this problem is by using a homogeneous and stiffer material.
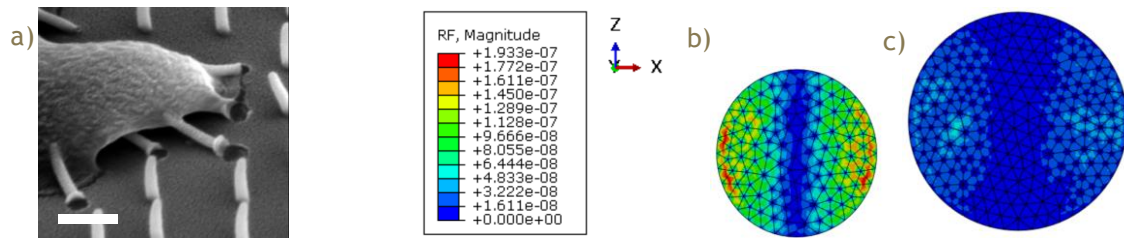
Figure 3-10 (a) The pillars are detached (50° tilted view with a scale bar of 250 nm). The reaction force of OST2 (b) and OST2-D50 (c) on the bottom of the pillar.

Computational modeling was also done for the OST1 pattern. The input value for the forces was 56.853 nN. It was assumed that the forces are distributed over the 300 x 300 nm pattern area. This assumption was made according to the spacing of OST2 nanopattern. The results show that the pillar is deflected 2.184 nm (Figure 3-11).
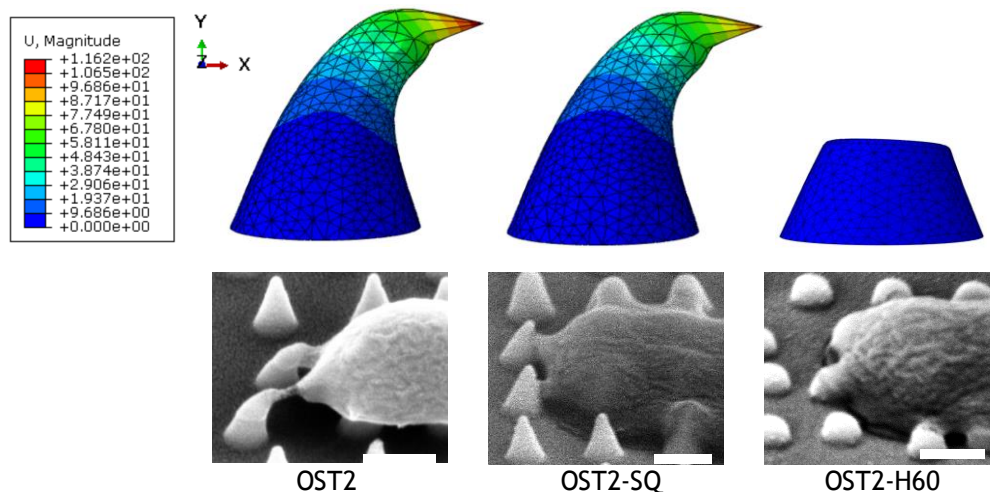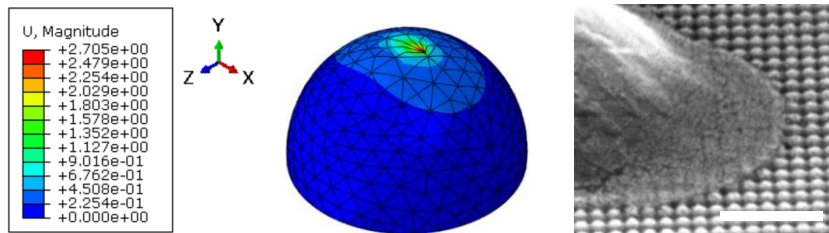

Figure 3-11 Comparison between OST1 pillar deflection in the simulation and SEM images (50° tilted view with scale bar of 250 nm)

4

Discussion

4.1 Bacterial Cells Adhesion on the Nanopatterns and the Role of EPS

When bacteria adhere on the surface, extracellular polymeric substance (EPS) is produced right away to help bacterial adhesion and provides protection [29]. EPS is a natural polymer consisting of polysaccharides, proteins, lipids, and DNA [30]. In the experiment, the projected area of EPS was measured. However, it is not known whether the pattern affects the production of EPS. This value does not resemble the production of EPS because the volume is unknown. The area information can give more understanding of the adhesion mechanism. According to the results, the *E. coli* form a different EPS arrangement depending on the surface they encountered.

In Table 4-1, the adhesion of *E. coli* on various surfaces is illustrated. On the smooth surface, such as CTR1 and CTR2 surfaces, the EPS can spread effortlessly. Bacteria and EPS can adhere everywhere without facing contact problem. On the OST1 pattern, the EPS has a larger area. The surface is densely patterned and EPS seems unable to seep between the pillars. In consequence, the EPS has to spread to increase the contact area and adhesion site. On the OST2, OST2-SQ, and OST2-D50, *E. coli* are struggling to attach on the patterns. It is shown by the low number of adherent bacteria on the nanopatterns. The spacing of the nanopillars is larger than the OST1 nanopattern. Thus, the bacteria have to secrete and stretch appendages of EPS. Due to high cohesive forces, some of the pillars bend. However, on the OST2-H60, the bacteria are less challenged than on the other OST2 patterns. Due to the lower height, the pattern provides a greater surface area and more attachment points for the EPS. In consequence, the bacteria can attach their EPS to the surrounding area.

The computational modeling showed that the bacteria and EPS exert shear forces in the order of 10^{-6} N to the pillars. However, this model is a simplification of the mechanism of *E. coli* and EPS attachment. The calculation was also based on the properties of EBID deposits and the displacement of the nanopillars, which are not entirely known and resulted in a big range of deviation. In the study conducted by Potthoff *et al*. [31], the adhesion force of *E. coli* was measured by detaching in the vertical direction using fluidic force microscopy (FluidFM) (Figure 4-1). The results indicated that the adhesion force was on the scale of 10^{-9} N.

Table 4-1 Illustration of bacterial cells adhesion on the control and nanopatterned surfaces. The green color indicates *the E. coli*, the yellow color indicates the EPS, and the grey colors indicates the available area of contact.

Control surface (CTR1 & CTR2)	OST1
OST2	OST2-SQ
OST2-H60	OST2-D50
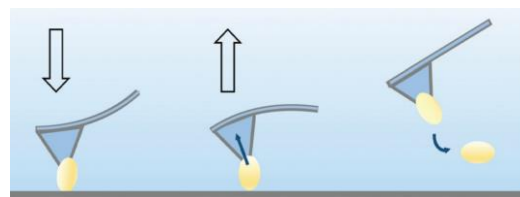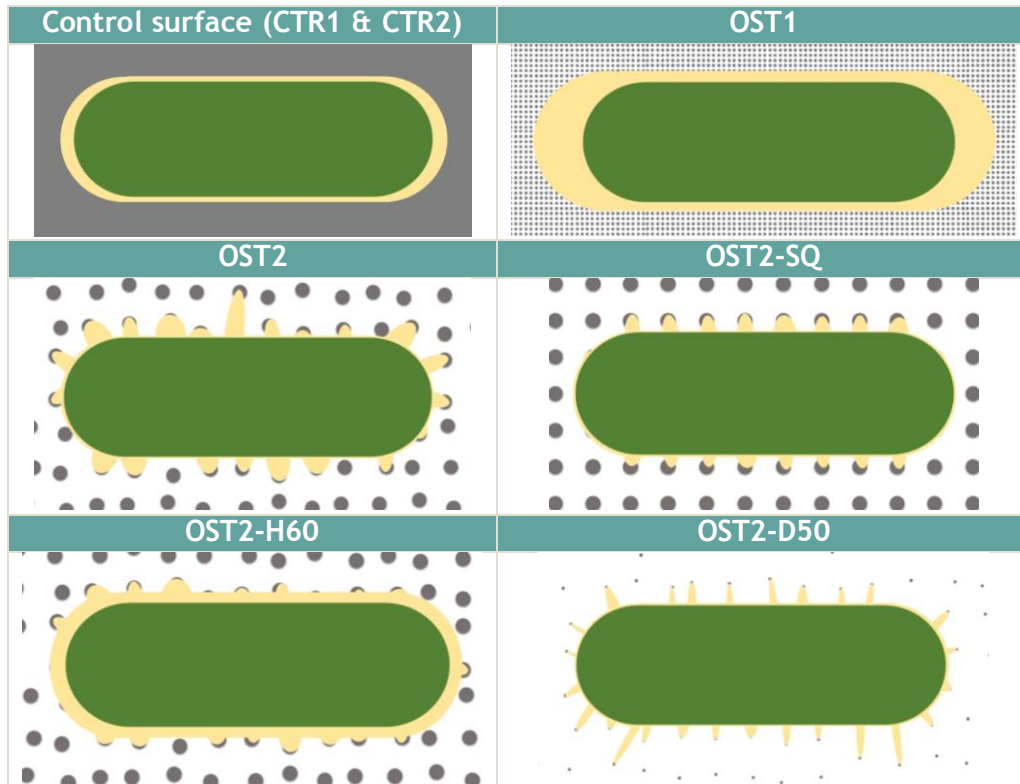
Figure 4-1 Illustration of bacteria detachment using FluidFM [31]

4.2 Nanopatterns-Induced Bactericidal Effects and Potential Mechanisms

The quantified results from the SEM images suggest that bactericidal properties only occur on the OST2, OST2-H60, and OST2-SQ nanopatterns. The results also show that the dominant factor in the bactericidal effect is the feature size of the nanopattern.

According to the SEM images, the mechanism of cell death on OST2 and OST-SQ nanopatterns may be an outcome from two local stresses occurring in the bacteria (Figure 4-2a). The first stress is induced by the size of the nanopillars. Most of the bactericidal surfaces that have been studied consist of pillars with an aspect ratio greater than 1 and sharp tip [16]. One of which is the wings of Clanger cicada (*P. claripennis*). A biophysical model was developed by Pogodin *et al.* [18], which suggests that the membrane is torn due to the local stress and non-uniform stretching induced by the nanopillars. The cell walls of bacteria are rigid and not elastic enough to follow the topography, resulting in irreversible membrane rupture and cytoplasm leakage.

26

The short-term experiment showed that the bactericidal activity was spontaneous and could take place within 5 minutes [32]. Moreover, a sharper tip also enhances the bactericidal activity [33]. The second bactericidal mechanism was proposed by Bandara *et al*. [34]. They indicated that the bactericidal activity could be induced by the strong adhesion between the EPS and the pillars. During the initial contact, the EPS "glues" onto the nanopillars to help the bacteria attach to the surface. High adhesive forces are developed between the pillars, EPS, and bacteria, resulting in separation between inner and outer membrane during bacterial motility (Figure 4-2b).
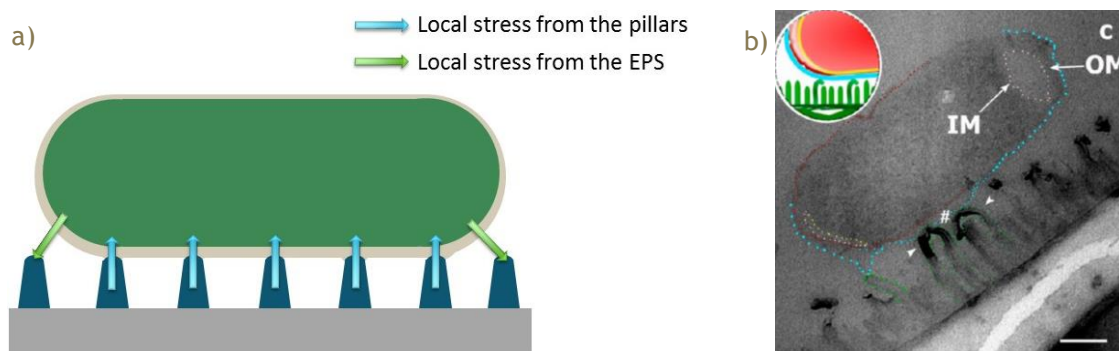
Figure 4-2 (a) Two mechanisms of cell death on OST2 nanopattern. (b) Cross-section TEM image of *E. coli* shows membrane separation due to high adhesive forces developed between the EPS and the pillars [34]

The bactericidal activity also occurred on the OST2-H60 pillars. The OST2-H60 had a flat top and lower height (~60 nm) than the OST2. The EPS can move under the bacteria and support the attachment (Figure 4-3a). Thus, the stress and stretching exert by the pillars might be lower and reduce the bactericidal activity. Shear stress is possibly the reason for killing mechanism on the OST2-H60 nanopattern (Figure 4-3b). Sahoo *et al*. [35-37] did an extensive study on the effect of shear stress on bacteria. The growth of bacteria was extremely affected by the shear stress. At a high shear rate, the viable cells in the cultivation decreased rapidly after 10 hours. They suggested that the shear stress experienced by bacteria is converted into biochemical signals. The shear stresses stimulate NADH oxidase (NOX), which leads to increased production of superoxide inside the cell. Due to the high level of reactive oxygen species (ROS) inside the bacteria, caspase-3-like protase (C3LP) is activated and resulting in cell death.

Figure 4-3 (a) 50° tilted SEM images of *E. coli* on OST2-H60 nanopattern (scale bar 1 μm). The arrow indicates the gap between the surface and bacteria filled with EPS. (b) Mechanism of cell death on OST2-H60 pattern.

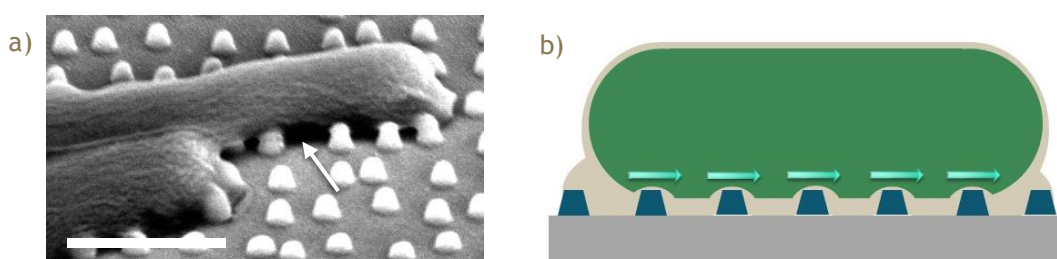On the OST2-H60 pillars, the shear forces occur right away after the *E. coli* adhered on the surface. The bacteria are exposed to the flat-top of the nanopillars. The shear stresses might be generated in the cells while the bacteria move around and divide. The density data indicated that the bacteria on OST2-H60 pattern are able to attach on the pattern. However, after a while, the bacteria start to experience cell death.

4.3 Nanopatterns with Desired Differential Effects on Stem Cells and Bacterial Cells

Designing a multibiofunctional surface is a great challenge because there is a huge difference between mammalian cells and bacteria adhesion. Cell attachment involves many signaling proteins and adhesomes [38]. The major receptors in cell-material interaction are integrins. Integrins facilitate the initial interaction between cell and material when the cells first reach the surface. Integrins act as mechanotransducer in the cell by translating extracellular mechanical stimulations into intracellular responses. When the cells encounter the surface topography, tensions occur and activate integrins (Figure 4-4a). The activation induces integrins clustering followed by protein recruitment and connection with the cell cytoskeleton [39]. Molecules are built up at their periphery, resulting in a focal adhesion.

On the other hand, bacterial adhesion is related to bacterial and surface charges. Two dominant interactions control the bacterial adhesion on the substrate [40]. The first interaction is van der Waals forces, which attract the bacteria to adhere. On the other hand, the repulsive electrostatic forces also occur. These forces repel each other, however, if attractive forces overweight repulsive forces, the bacteria will approach the surface (Figure 4-4b). When the bacteria arrive on the surface, the bacteria develop extracellular polymeric substance (EPS), and the attachment becomes irreversible. The presence of topography, may change the surface wettability of the materials. Superhydrophobic surface is often connected with the anti-biofouling effect [16], which can prevent the adhesion of bacteria. Physical and mechanical mechanisms seem to play a role on specific topographies.
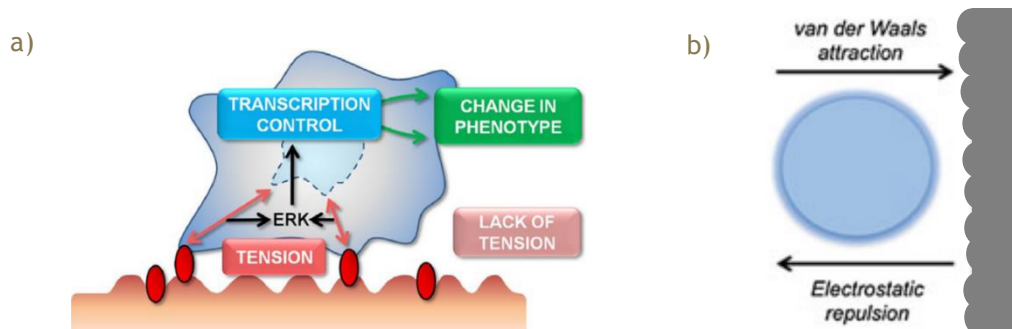
Figure 4-4 (a) Topography affects adhesion, tension, and signaling of mammalian cells. [39] (b) Overview of the forces influencing bacterial attachment to surfaces [40]

In this study, the feature sizes of the nanopatterns were chosen based on their performance in stimulating MSCs adhesion and osteogenic differentiation. Based on the previous studies, MSCs and OPGs had the greatest adhesion and differentiation on OST1 nanopattern relative to higher pillars [6-7] (Figure 4-5). The 15 nm-high pillars could

enhance the localized cue and stimulate the protein interaction in the cells. However, in this study, the OST1 pattern is not the best candidate for antibacterial properties. Although the OST1 nanopattern has an inhibitory effect on bacterial adhesion, it did not show bactericidal properties.

Amongst all the nanopatterns investigated in this thesis, the bactericidal properties only occurred on OST2, OST2-H60, and OST2-SQ nanopatterns. These nanopatterns had much larger diameter and height than the OST1. OST2 shares comparable features with the osteogenic pattern previously mentioned by Dalby *et al.* [11]. The nanopatterns had the same diameter and lateral arrangement. This pattern can be therefore considered a good candidate for providing multibiofunctional surface. The OST2-SQ nanopattern did not show better bactericidal activity than OST2 and OST-H60 nanopatterns. The ordered arrangement also did not stimulate the osteogenic differentiation [11]. Thus, it is not a potential candidate. However, it showed that controlled disorder is an important factor in controlling MSCs and bacterial cells behaviors, which is not shown in the previous study. The only difference between OST2 and OST2-H60 are the height and the shape of the nanopillars. The height of OST2-H60 may be beneficial for MSCs as the trend indicates that the lower height had a greater osteogenic differentiation (Figure 4-5) [6]. In addition, the results showed that bactericidal activity occurred at the lower height, smaller aspect ratio, and in the absence of the sharp tip morphology.
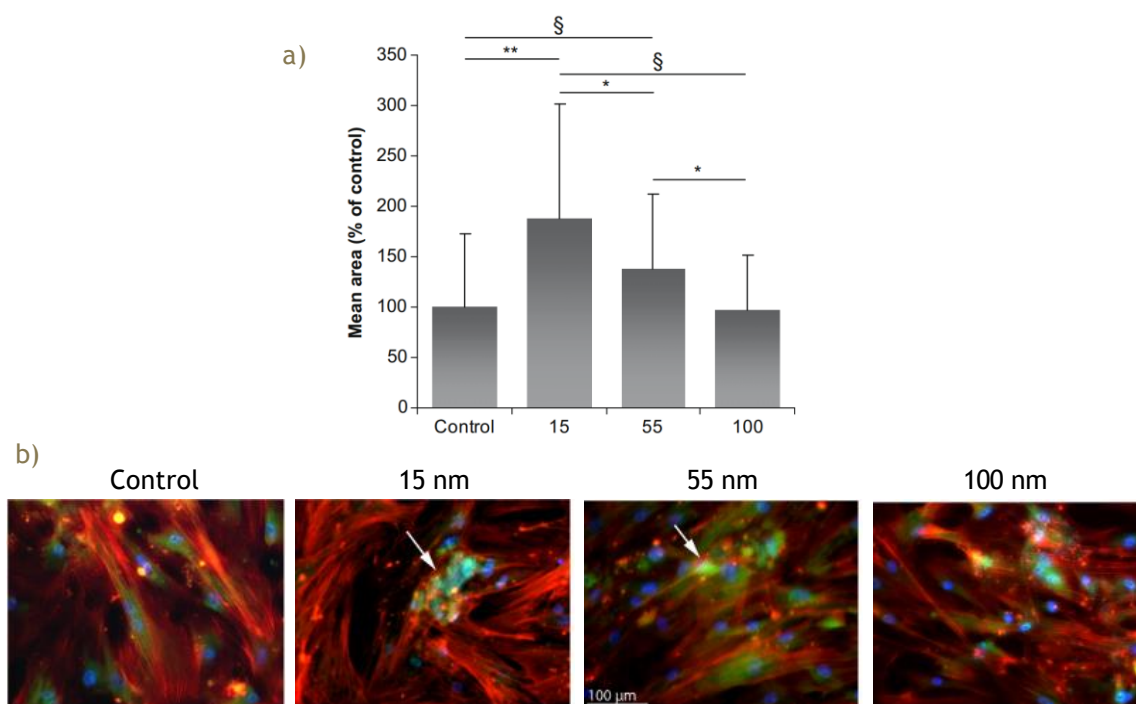

Figure 4-5 (a) Graph illustrating the adhesion area of MSCs between different surfaces [6]. (b) The fluorescence images were obtained after 21 days culture. Red color represents actin, green color represents osteopontin (expression of osteogenic markers), and blue color represents the nucleus. The arrows indicate osteogenic nodule formation. [6]

5

Conclusions and Outlook

Five nanopatterns were evaluated in this thesis. Based on the quantified results from SEM images, all of the nanopatterns, except OST2-H60, gave a great effect in reducing bacterial adhesion. Moreover, OST2, OST2-H60, and OST2-SQ nanopatterns exhibited bactericidal activities. The results also suggested that the controlled disordered arrangement caused more bactericidal activity than the square array. Distinct bactericidal mechanisms were proposed. On the OST2 and OST2-SQ nanopatterns, the bacteria might experience non-uniform stretching of the cell wall and membrane separation due to the local stresses from the pillars and the EPS-pillars adhesion. On the other hand, on the OST2-H60 nanopattern, the death probably due to a high shear stress induced by the flat-top area of the pillars. These findings suggested that nanopatterns with osteogenic and antibacterial properties can be developed.

For the future study, there are several additional experiments in order to understand the bactericidal mechanism of the nanopatterns; such as short- and long-term experiment, and assessment using fluorescence microscopy and FluidFM. The short-term experiment can give information about when the bactericidal activity occurred, whether it is spontaneously or at extended duration. On the other hand, the long-term experiment will provide information about bacterial growth and biofilm formation on the patterns. By using fluorescence microscope and FluidFM, live cells imaging can be performed. In addition, extra information about the viability and adhesion force can be acquired. In order to evaluate the bactericidal properties of the patterns, experiment using the same surfaces with different types of bacterial cells should be done. *Staphylococcus aureus* and *Staphylococcus epidermidis* are the major pathogens that frequently found in the implant-related infection in orthopedics. By performing an *in vitro* study using these bacteria, the experiment will be more representing the actual condition. Moreover, human cell, for example, MSCs or osteoblasts, should be introduced into the experiment. Thus, the behavior of the cells on the nanopatterns can be assessed.

References

[1] M. Ribeiro, F. J. Monteiro and M. P. Ferraz, "Infection of orthopedic implants with emphasis on bacterial adhesion process and techniques used in studying bacterial-material interactions," *Biomatter,* vol. 2, no. 4, pp. 176-194, 2012.

[2] Y. Wang, G. Subbiahdoss, J. Swartjes, H. C. van der Mei, H. J. Busscher and M. Libera, "Length-Scale Mediated Differential Adhesion of Mammalian Cells and Microbes," *Advanced functional materials,* vol. 21, pp. 3916-3923, 2011.

[3] W. J. Peace, "Ortho Info," October 2012. [Online]. Available: http://orthoinfo.aaos.org/topic.cfm?topic=A00629. [Accessed 6 June 2017].

[4] S. Dobbenga, L. E. Fratila-Apachitei and A. A. Zadpoor, "Nanopattern-induced osteogenic differentiation of stem cells – A systematic review," *Acta Biomaterialia,* vol. 46, pp. 3-14, 2016.

[5] Database Center for Life Science (DBCLS), "Togo Picture Gallery," [Online]. Available: http://togotv.dbcls.jp/ja/pics.html. [Accessed 19 September 2017].

[6] T. Sjostrom, M. J. Dalby, A. Hart, R. Tare, R. O. C. Oreffo and B. Su, "Fabrication of pillar-like titania nanostructures on titanium and their interactions with human skeletal stem cells," *Acta biomaterialia,* vol. 5, pp. 1433-1441, 2009.

[7] L. E. McNamara, T. Sjostrom, K. E. V. Burgess, J. J. W. Kim, E. Liu, S. Gordonov, P. V. Moghe, R. M. D. Meek, R. O. C. Oreffo, B. Su and M. J. Dalby, "Skeletal stem cell physiology on functionally distinct titan ia nanotopographies," *Biomaterials,* vol. 32, pp. 7403-7410, 2011.

[8] T. Sjostrom, L. E. McNamara, R. M. D. Meek, M. J. Dalby and B. Su, "2D and 3D Nanopatterning of Titanium for Enhancing Osteoinduction of Stem Cells at Implant Surfaces," *Advance Healthcare Materials,* vol. 2, pp. 1285-1293, 2013.

[9] S. E. Maclaine, N. Gadhari, R. Pugin, R. M. D. Meek, M. Liley and M. J. Dalby, "Optimizing the Osteogenicity of Nanotopography Using Block Co-Polymer Phase Separation Fabrication Techniques," *Journal of Othopaedic Research,* pp. 1190-1197, 2012.

[10] M. J. Dalby, D. McCloy, M. Robertson, C. D. W. Wilkinson and R. O. C. Oreffo, "Osteoprogenitor response to defined topographies with nanoscale depths," *Biomaterials,* Vols. 1306-1315, p. 27, 2006.

[11] M. J. Dalby, N. Gadegaard, R. Tare , A. Andar, M. O. Riehle, P. Herzyk, C. D. W. Wilkinson and R. O. C. Oreffo, "The control of human mesenchymal cell differentiation using nanoscale symmetry and disorder," *Nature Materials,* vol. 6, pp. 997-1003, 2007.

[12] L. Jin, W. Guo, P. Xue, H. Gao, M. Zhao, C. Zheng, Y. Zhang and D. Han, "Quantitative assay for the colonization ability of heterogeneous bacteria on controlled nanopillar structures," *Nanotechnology,* vol. 26, no. 055702, 2015.

[13] L.-C. Xu and C. A. Siedlecki, "Submicron-textured biomaterial surface reduces staphylococcal bacterial adhesion and biofilm formation," *Acta Biomaterialia,* vol. 8, pp. 72-81, 2012.

[14] M. N. Dickson, E. I. Liang, L. A. Rodriguez, N. Vollereaux and A. F. Yee, "Nanopatterned polymer surfaces with bactericidal properties," *Biointerphases,* vol. 10, no. 021010, 2015.

[15] V. T. H. Pham, V. K. Truong, A. Orlowska, S. Ghanaati, M. Barbeck, P. Booms, A. J. Fulcher, C. M. Bhadra, R. Buividas, V. Baulin, C. J. Kirkpatrick, P. Doran, D. E. Mainwaring, S. Juodkazis, R. J. Crawford and E. P. Ivanova, """ Race for the Surface" : Eukaryotic Cells Can Win," *ACS Applied Materials & Interfaces,* vol. 8, pp. 22025-22031,

2016.

[16] A. Tripathy, P. Sen, B. Su and W. H. Briscoe, "Natural and bioinspired nanostructured bactericidal surfaces," *Advances in Colloid and Interface Science,* 2017.

[17] X. Li and T. Chen, "Enhancement and suppression effects of a nanopatterned surface on bacterial adhesion," *Physical review,* vol. 93, no. 052419, 2016.

[18] S. Pogodin, J. Hasan, V. A. Baulin, H. K. Webb, V. K. Truong, T. H. P. Nguyen, V. Boshkovikj, C. J. Fluke, G. S. Watson, J. A. Watson, R. J. Crawford and E. P. Ivanova, "Biophysical Model of Bacterial Cell Interactions with Nanopatterned Cicada Wing Surfaces," *Biophysical Journal,* vol. 104, pp. 835-840, 2013.

[19] E. P. Ivanova, J. Hasan , H. K. Webb, V. K. Truong, G. S. Watson, J. A. Watson, V. A. Baulin, S. Pogodin, J. Y. Wang, M. J. Tobin, C. Lobbe and R. J. Crawford, "Natural Bactericidal Surfaces: Mechanical Rupture ofPseudomonas aeruginosa Cells by Cicada Wings," *Small,* vol. 8, no. 16, pp. 2489-2494, 2012.

[20] L. Hirt, A. Reiser, R. Spolenak and T. Zambelli, "Additive Manufacturing of Metal Structures at the Micrometer Scale," *Advanced materials,* vol. 29, no. 1604211, 2017.

[21] J. Fiedler, B. Ozdemir, J. Bartholoma, A. Pletti, R. E. Brenner and P. Ziemann, "The effect of substrate surface nanotopography on the behavior of multipotent mesenchymal stromal cells and osteoblasts," *Biomaterials,* vol. 34, pp. 8851-8859, 2013.

[22] W. F. van Dorp and C. W. Hagen, "A critical literature review of focused electron beam induced deposition," *Journal of applied physics,* vol. 14, no. 081301, 2008.

[23] S. G. Rosenberg, K. Landheer, C. W. Hagen and D. H. Fairbrother, "Substrate temperature and electron fluence effects on metallic films created by electron beam induced deposition," *Journal of Vacuum Science & Technology B,* vol. 30, no. 5, 2012.

[24] H. Plank, C. Gspan, M. Dienstleder, G. Kothleitner and F. Hofer, "The influence of beam defocus on volume growth rates for electron beam induced platinum deposition," *Nanotechnology,* vol. 19, no. 485302, 2008.

[25] W. M. Sigmund and S.-H. Hsu, "Cassie-Baxter model," in *Encyclopedia of Membranes,* Berlin, Springer, 2016, pp. 310-311.

[26] M. Sun, G. S. Watson, Y. Zheng, J. A. Watson and A. Liang, "Wetting properties on nanostructured surfaces of cicada wings," *The journal of experimental biology,* vol. 212, pp. 3148-3155, 2009.

[27] S. Okada, T. Mukawa, R. Kobayashi, M. Ishida, Y. Ochiai, T. Kaito, S. Matsui and J.-i. Fujita, "Comparison of Youn g's Modulus Dependency on Beam Acce lerating Voltage between Electron-Beam - and Focused Ion-Beam-Induced Chemical Vapor Deposition Pillars," *Japanese journal of applied physics,* vol. 45, no. 6B, pp. 5556-5559, 2006.

[28] W. Ding, D. A. Dikin, X. Chen, R. D. Piner, R. S. Ruoff, E. Zussman, X. Wang and X. Li, "Mechanics of hydrogenated amorphous carbon deposits from electron-beam-induced deposition of a paraffin precursor," *Journal of applied physics,* vol. 98, no. 014905, 2005.

[29] H.-C. Flemming, "The perfect slime," *Colloids and Surfaces B: Biointerfaces,* vol. 86, pp. 251-259, 2011.

[30] H.-C. Flemming and J. Wingender, "The biofilm matrix," *Nature reviews microbiology,* vol. 8, p. 623, 2010.

[31] E. Potthoff, D. Ossola, T. Zambelli and J. A. Vorholt, "Bacterial adhesion force quantifi cation by fluidic force microscopy," *Nanoscale,* vol. 7, no. 4070, pp. 4070-4079, 2015.

[32] E. P. Ivanova, J. Hasan , H. K. Webb, V. K. Truong, G. S. Watson, J. A. Watson, V. A. Baulin, S. Pogodin, J. Y. Wang, M. J. Tobin, C. Lobbe and R. J. Crawford, "Natural Bactericidal Surfaces: Mechanical Rupture of Pseudomonas aeruginosa Cells by Cicada Wings," *Small,* vol. 8, no. 16, pp. 2489-2494, 2012.

[33] S. M. Kelleher, O. Habimana, J. Lawler, B. O' Reilly, S. Daniels, E. Casey and A. Cowley, "Cicada Wing Surface Topography: An Investigation into the Bactericidal Properties of

Nanostructural Features," *ACS Applied Materials and Interfaces,* vol. 8, pp. 14966-14974, 2016.

[34] C. D. Bandara, S. Singh, I. O. Afara, A. Wolff, T. Tesfamichael, K. Ostrikov and A. Oloyede, "Bactericidal Effects of Natural Nanotopography of Dragonfl y Wing on Escherichia coli," *ACS Applied Materials and Interfaces,* vol. 9, pp. 6746-6760, 2017.

[35] S. Sahoo, R. K. Verma, A. K. Suresh, K. K. Rao, J. Bellare and G. K. Suraishkumar, "Macro-Level and Genetic-Level Responses of Bacillus subtilis to Shear Stress," *Biotechnology progress,* vol. 19, no. 6, 2003.

[36] S. Sahoo, K. Krishnamurthy Rao, A. K. Suresh and G. K. Suraishkumar, "Intracellular Reactive Oxygen Species Mediate Suppression of Sporulation in Bacillus subtilis Under Shear Stress," *Biotechnology and bioengineering,* vol. 87, no. 1, 2004.

[37] S. Sahoo, K. K. Rao and G. K. Suraishkumar, "Reactive Oxygen Species Induced by Shear Stress Mediate Cell Death in Bacillus subtilis," *Biotechnology and Bioengineering,* vol. 94, no. 1, 2006.

[38] P. M. Tsimbouri, L. E. McNamara, E. V. Alakpa, M. J. Dalby and L.-A. Turner, "Cell–Material Interactions," in *Tissue Engineering.,* Elsevier, 2015, pp. 217-251.

[39] H. J. Anderson, J. K. Sahoo, R. V. Ulijn and M. J. Dalby, "Mesenchymal stem cell fate: applying biomaterials for control of stem cell behavior," *Frontiers in bioengineering and biotechnology,* vol. 4, no. 38, 2016.

[40] S. Aguayo and L. Bozec, "Mechanics of Bacterial Cells and Initial Surface Colonization," in *Biophysics of Infection*, Cham, Springer, 2016, pp. 245-260.

Appendix A
Principle of EBID

EBID is performed in electron microscopes, mostly scanning electron microscopes (SEM) or transmission electron microscopes (TEM). A gas precursor is delivered using gas injection system (GIS) (Figure 1a). The precursor contains atoms of the material to be deposited. As the gas precursor entering the chamber, the gas immediately adsorbs onto the surface of the substrate. Exposing the substrate with precursor molecules to a focused electron beam, the precursor molecules are dissociated resulting in volatile and nonvolatile fragments, where the non-volatile components adhere onto the surface (Figure 1e). EBID deposits the material molecule by molecule, resulting in an amorphous composite structure contained metal and carbon [1] (Figure 1-b).
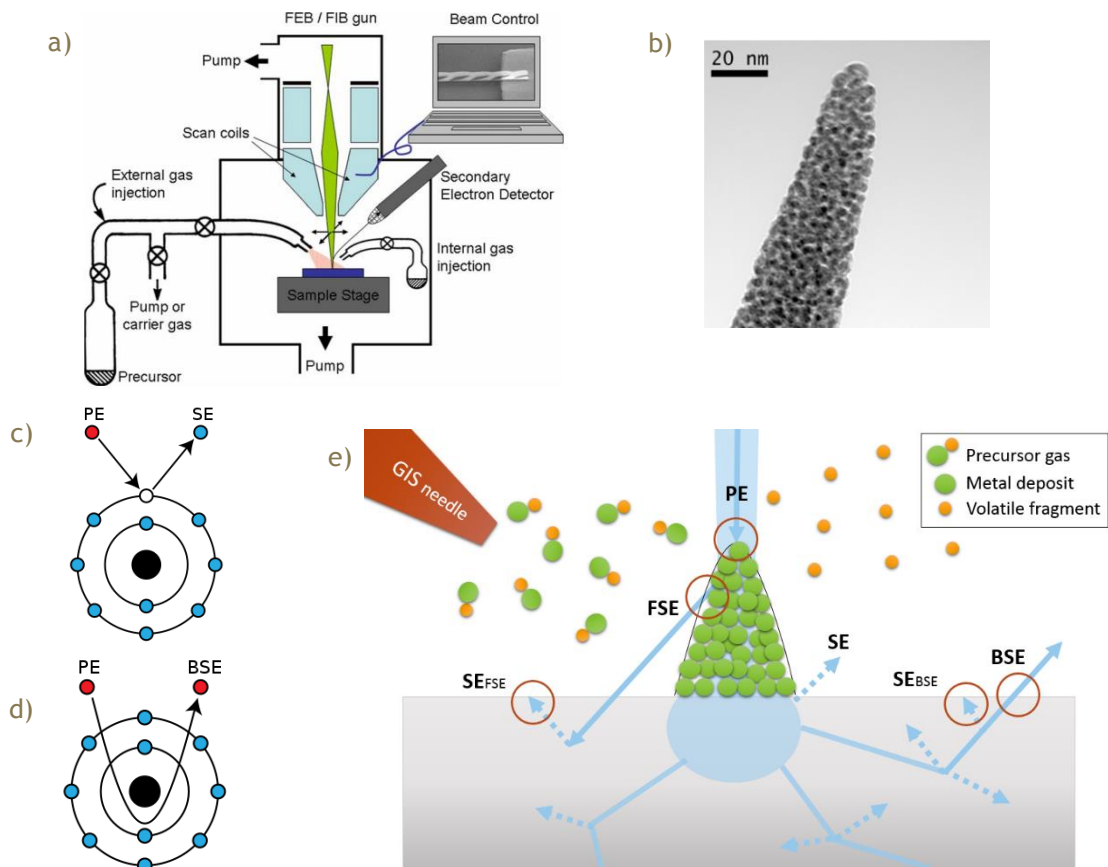

Figure 1 (a) Schematics of FIB and FEB nanofabrication systems. GIS with external and internal precursor reservoirs are shown [2]. (b) TEM image of $C_9H_{16}Pt$ deposit [3]. (c) Secondary electrons are knocked out due to an inelastic collision [4]. (d) Elastic collision generates backscattered electrons [4]. (e) Schematic drawing of deposition and electron scattering. Molecules are adsorbed on the surface. Dissociation under electron impact resulting in metal deposition (non-volatile) and volatile fragment. The primary electrons scatter into secondary electrons, backscattered electrons, and forward-scattered electrons.

The primary electrons (PEs) collide with the sample's atom in an elastic and inelastic manner. In an elastic collision, the atom's structure is roughly changed, and the energy is conserved, whereas in an inelastic collision, there is electron excitation and an energy loss. The PEs that collided inelastically knock an electron out. These displaced electrons are called secondary electrons (SEs) and have an energy lower than 50 eV (Figure 1c). SEs are the major player in determining the resolution. SEs mostly occur near the surface and produce edge broadening of the structure. It deposits sidewall and continuously occurs until it is no longer able to exit from the structure. In an elastic collision, the PEs generate backscattered electrons (BSEs) (Figure 1d). The energy of BSEs is typically more than 50 eV. Due to its high energy, BSEs can travel within the substrate and provoke proximity effects which induce deposition outside the targeted beam area. As the structure grows, PEs also shatter because of the collision with deposited material. Forward scattered electrons (FSEs) are additionally generated, making the proximity effect takes more influence in the process (Figure 1e).

There are several variables that was prearranged in the EBID process, namely: 1) Patterning regime, 2) Beam current, 3) Beam accelerating voltage, 4) Chamber vacuum, and 5) Duration of exposure. However, in reality, there are other variables that influence the deposition process.

1) Patterning regime

There are two patterning conditions; 1) Electron-limited regime, and 2) Precursor-limited regime [1]. In the electron-limited regime, there is an abundant supply of precursor gas. The molecule replenishment rate is higher than the dissociation rate. Thus, the growth is only affected by the number of electrons hitting the surface. In the experiment, electron-limited regime can be characterized by exposing the substrate in a different dwell time. The size of the deposition will be linearly dependent on the dwell time (Figure 2a). On the other hand, in the precursor-limited regime, there is a limited amount of precursor gas to be dissociated. The growth saturates independently from the current density (Figure 2b). In this regime, the growth is highly determined by the surface diffusion and gas molecule adsorption. To increase the deposition rate, the irradiation area has to be decreased.
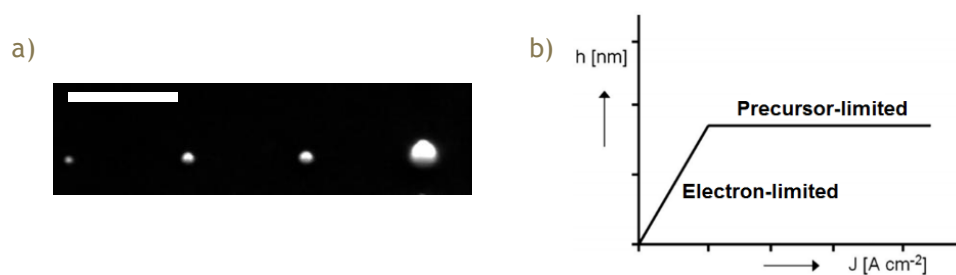

Figure 2 (a) An escalation of growth as the dwell time increases (25° tilted SEM images, scale bar 300 nm). (b) Schematic of the deposit height h as a function of J (electric current density), shows the electron- and precursor-limited regimes [1]

2) Beam current

Beam current is defined as the number of electrons that passes from the electron column. The beam current is proportional to the beam diameter [1]. A higher current means that there are more electrons traveling through the column. Due to the increasing number of PEs, the beam diameter is broader. As the number of electrons and irradiation area increases, more molecules are dissociated. This leads to higher concentrations of nonvolatile components in the deposit.

3) Accelerating voltage

Beam accelerating voltage is an energy difference between the electron gun and the substrate. With a higher accelerating voltage, the PEs will travel with higher velocity from the electron column. As the PEs hit the surface, the PEs will penetrate deeper and the collusion area will be larger (Figure 3a). Thus, it will result in an increase of BSE generation and a greater proximity effect [5].
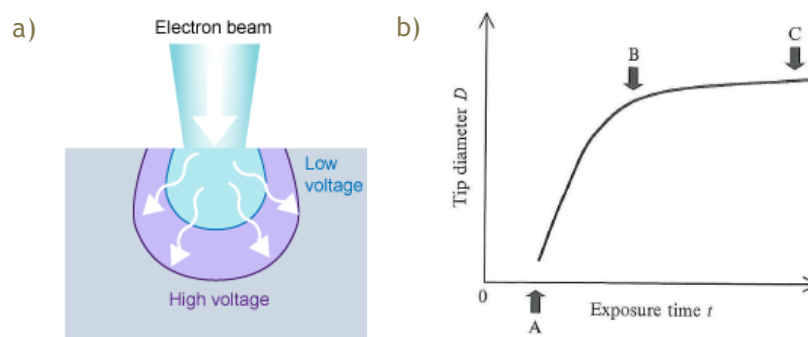
Figure 3 (a) Illustration low and high acceleration voltage that are penetrated on the substrate [5]. (b) Tip diameter as a function of exposure time. Growth starts with the nucleation phase (0-A), followed by a fast growth stage (A-B) and ends with saturation (B-C) [6]

4) Chamber vacuum

In order to minimize the scattering of the electron beam before reaching the specimen, the EBID should be performed in a high vacuum environment [4]. This set-up is also advantageous in the deposition process. Due to the high vacuum, the chamber is "clean", and the content of water vapor and hydrocarbons are less, leading to purer deposits [5].

5) Duration of exposure

In the single dot exposure, the pattern is made of discrete point or pixel. The duration of the beam exposure on each point is called dwell time (t_{dwell}). It is mostly ranging from 1 µs to 10 ms. When the exposure starts, the PEs are traveling from the column to the substrate. After a certain time (Figure 3b, point A), the PEs hit the surface and the nucleation starts. SEs are scattered around the beam diameter area, resulting in a lateral growth. From point A to B, PEs and SEs dissociate the molecules in a fast pace. As the tip grows, PEs penetrate from the apex of the tip. SEs are scattered inside the structure resulting in a sidewall deposition. The lateral growth starts slowing down because SEs are hard to escape from the structure (Figure 3b, point B). The maximum diameter is reached due to SEs no longer being able to escape from the tip (Figure 3b, point C) [6].

In order to prevent growth saturation, a delay/blanking must occur between the dwell times to replenish the precursor molecules. This method is also used to avoid the transition from electron-limited regime to precursor-limited regime. The duration of blanking is called refresh time ($t_{refresh}$). In this thesis, there were two types of blanking terms, which are called repetitions and passes (Figure 4). By using the repetition, the beam was kept staying on the particular position and repeating the exposure. After it was complete, the beam moved to the following coordinates. After finishing one loop of patterning, the system might need to expose the exposure all over again. The number of passes defined the how many times the system has to carry out this loop. If the streamfile contains 50 repeats and 3 passes, it means that in every loop, the beam needs to exposure 50 times, and the loop had to be executed 3 times. Thus, the total number of blanking on every point is 150 times.
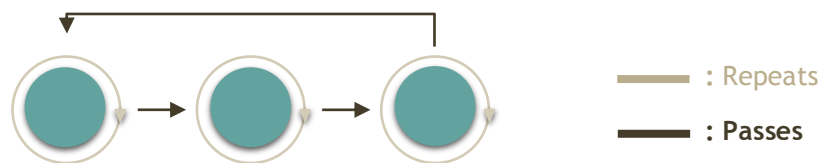

: Repeats

: **Passes**

Figure 4 Schematic representation of repeats and passes

References

[1]   W. F. van Dorp and C. W. Hagen, "A critical literature review of focused electron beam induced deposition," *Journal of applied physics,* vol. 14, no. 081301, 2008.

[2]   Utke Io, P. Hoffman and J. Melngailis, "Gas-assisted focused electron beam and ion beam processing and fabrication," *Journal of vacuum science and technology,* vol. 26, no. 4, 2008.

[3]   H. Plank, C. Gspan, M. Dienstleder, G. Kothleitner and F. Hofer, "The influence of beam defocus on volume growth rates for electron beam induced platinum deposition," *Nanotechnology,* vol. 19, no. 485302, 2008.

[4]   R. Hurt, "Wikipedia," 27 August 2016. [Online]. Available: https://commons.wikimedia.org/wiki/File:Electron_emission_mechanisms.svg. [Accessed 3 March 2017].

[5]   Australian microscopy & microanalysis research facility, "MyScope," 15 April 2014. [Online]. Available: http://www.ammrf.org.au/myscope/sem/. [Accessed 10 March 2017].

[6]   N. Silvis-Cividjian and C. W. Hagen, Adcances in imaging and electron physics volume 143: Electron-beam-induced nanometer-scale deposition, London: Elsevier, 2006.

Appendix B
Escherichia coli and Optimization of Experimental Protocols

Escherichia coli or *E. coli* is a bacteria that living inside human gastrointestinal tract. *E. coli* is one of pathogens in orthopedic implant infection [1]. It has been extensively studied and used as a model organism. E. coli has a rod-like shape with approximately 2.5 μm long and 0.8 μm in diameter. Under ideal condition, it can reproduce roughly every 20-30 minutes [2,3]. *E. coli* is classified as Gram-negative bacteria. The cell walls of gram-negative bacteria is thinner than the gram-positive bacteria. The cell walls consist of peptidoglycan which contributes in defining the shape and giving structural strength to bacteria. Outside the peptidoglycan, the gram-negative bacteria is protected by outer membrane. Lipopolysaccharides (LPS) is the main component of the outer membrane. It is a highly charged molecule and responsible for the negative charge of the gram-negative bacteria [4]. The illustration of the envelope structure of Gram-negative bacteria is presented in the figure below.
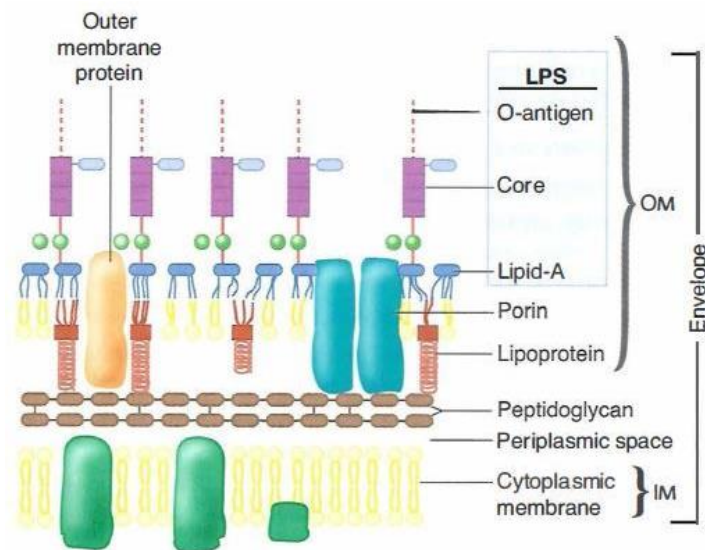

Figure 1 Envelope structure of Gram-negative bacteria

Before starting the experiment with the nanopatterns, the growth of *E. coli* in Lysogeny-broth (LB) medium was firstly analyzed. The silicon wafer samples were put inside the 24-well cell culture. Then, the samples were immersed in 1 mL of bacterial suspension and incubated at 37°C. There were two starting optical density, OD_{600} 0.05 and 0.01. The total incubation time was 5.5 hours. The optical density of the bacterial suspension was measured every 30 minutes. The growth curve is illustrated in the Figure 2a. The graph showed an exponential growth of *E. coli*. The growth is more or less resembled growth curve from the previous study [3]. The low magnification SEM images in the Figure 2b show the bacterial adhesion on the silicon wafer. As the incubation time increase, the number of bacterial adherent also rising.
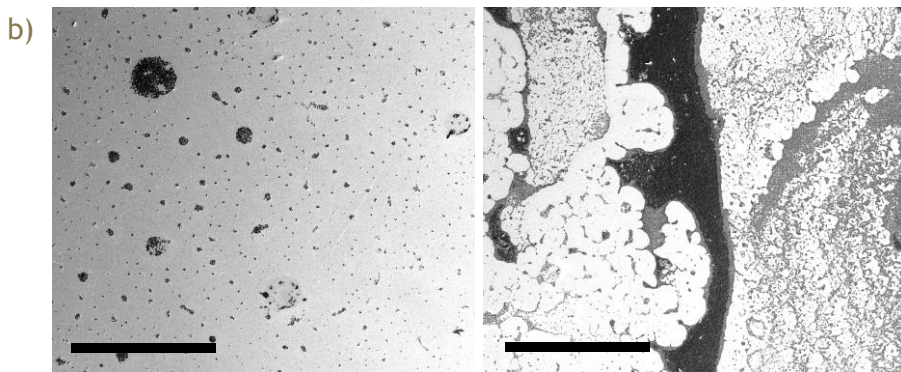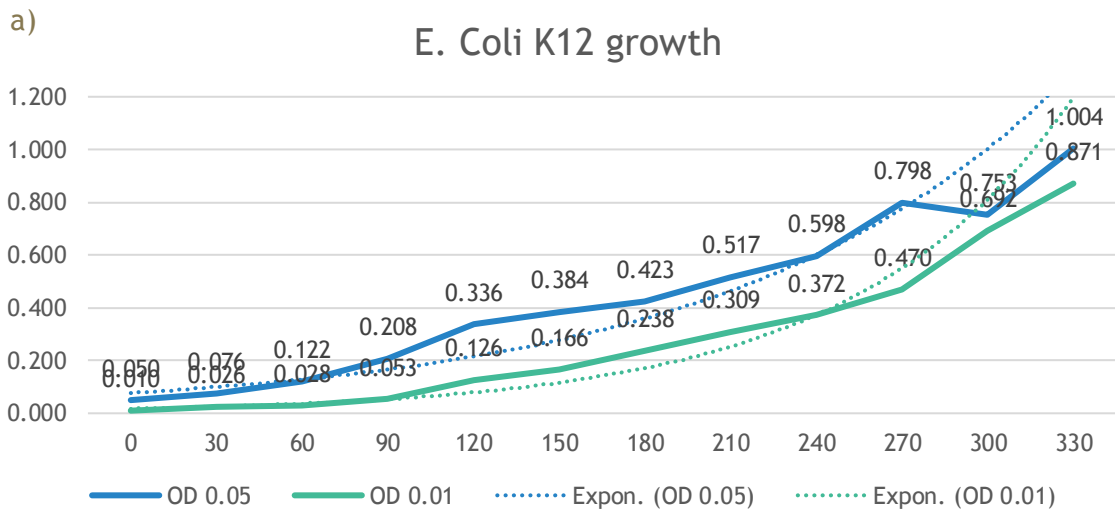
a)

Figure 2 (a) Growth curve of *E. coli* with starting OD_{600} of 0.05 and 0.01. (b) SEM images of *E. coli* with a shorter (left) and longer (right) incubation time. Black color indicates the bacteria and the grey color indicates the silicon substrate. Top view, scale bar 300 µm.

In order to eliminate the bacteria that not well adhered, washing process was implemented into the protocol. Silicon wafer was incubated with the bacterial suspension (OD_{600} 0.05) at 37°C for 18 hours. Two types of chemical used for washing, which are phosphate buffered saline (PBS) 0.01 M (pH 7.4) and MiliQ were analyzed. According to the SEM results, the bacteria formed aggregates after the sample was rinsed with MiliQ (Figure 3a). However, by using PBS for washing process, the cells were washed off and showed a better result (Figure 3b). PBS was the most appropriate chemical for washing the samples. PBS has a similar salinity level with the bacteria and does not induce the cell bursting due to osmotic flow [5].
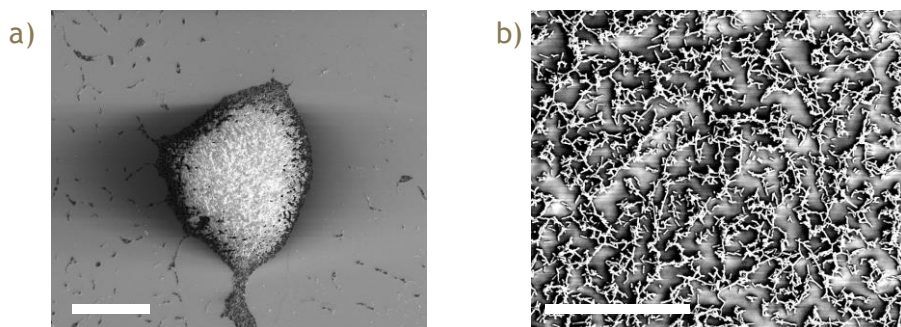
a)

b)

Figure 3 SEM images of *the E. coli* washed with MiliQ (a) and PBS (b). Charging was occurred on the image due to the aggregation of the bacteria. Top view, scale bar 50 µm.

42

Two control surfaces, silicon (CTR1) and platinum-carbon surface (CTR2), were incubated using *E. coli*. SEM images were taken after bacteria incubation (Figure 4 and 5). Cell morphology and density were measured and presented in Table 1.

Table 1 Cell length, cell width, percent increase of EPS area, and cell density of the silicon wafer (CTR1) and platinum-carbon surface (CTR2)

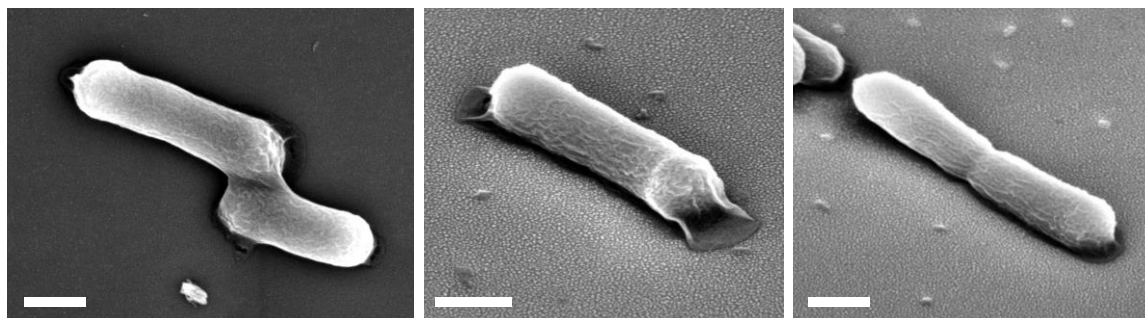| Surface	Cell length (µm)	Cell width (nm)	EPS area	Cell density (cell/µm^2)
CTR1	1.67 ± 0.44	485.22 ± 83.90	24.08 ± 10.90%	0.1849
CTR2	2.47 ± 0.62	694.08 ± 93.54	32.81 ± 3.94%	0.1701

Figure 4 SEM images of *E. coli* adhesion on silicon wafer (CTR1). Taken from the top (left image) and 50° tilted (middle and right images) with a scale bar of 500 nm.
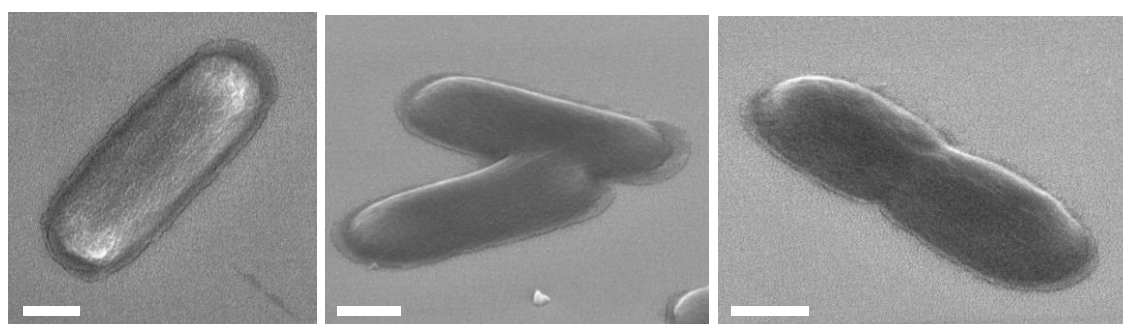

Figure 5 SEM images of *E. coli* adhesion on platinum-carbon surface (CTR2). Taken from the top (left image) and 50° tilted (middle and right images) with a scale bar of 500 nm.

References

[1] M. Ribeiro, F. J. Monteiro and M. P. Ferraz, "Infection of orthopedic implants with emphasis on bacterial adhesion process and techniques used in studying bacterial-material interactions," *Biomatter,* vol. 2, no. 4, pp. 176-194, 2012.

[2] H. C. Berg, "Why E. coli?," in *E. coli in motion*, New Yor, Springer, 2004, p. 1.

[3] G. Szonov, D. Joseleau-Petit and R. D'Ari, "Escherichia coli Physiology in Luria-Bertani Broth," *Journal of bacteriology,* vol. 189, no. 23, pp. 8746-8749, 2007.

[4] M. R. J. Salton and K.-S. Kim, "Structure," in *Medical Microbiology*, Galveston, University of Texas Medical Branch at Galveston, 1996.

[5] S. Das and H. R. Dash, "Application of molecular microbiology," in *Microbial biotechnology - a laboratory manual for bacterial system*, Odisha, Springer, 2015, p. 203.